TOI-836: A super-Earth and mini-Neptune transiting a nearby K-dwarf

Faith Hawthorn, Daniel Bayliss, Thomas G. Wilson, Andrea Bonfanti, Vardan Adibekyan, Yann Alibert, Sérgio G. Sousa, Karen A. Collins, Edward M. Bryant, Ares Osborn, et al.

Monthly Notices of the ROYAL ASTRONOMICAL SOCIETY

MNRAS **520,** 3649–3668 (2023) https://doi.org/10.1093/mnras/stad306
Advance Access publication 2023 February 9

TOI-836: A super-Earth and mini-Neptune transiting a nearby K-dwarf

Faith Hawthorn [1,2]★ Daniel Bayliss [1,2]★ Thomas G. Wilson [3]★ Andrea Bonfanti,[4] Vardan Adibekyan,[5,6] Yann Alibert,[7] Sérgio G. Sousa [5,6] Karen A. Collins [8] Edward M. Bryant [1,2] Ares Osborn [1,2] David J. Armstrong [1,2] Lyu Abe,[9] Jack S. Acton [10] Brett C. Addison [11] Karim Agabi,[9] Roi Alonso,[12,13] Douglas R. Alves [14] Guillem Anglada-Escudé,[15,16] Tamas Bárczy,[17] Thomas Barclay,[18,19] David Barrado,[20] Susana C. C. Barros,[5,6] Wolfgang Baumjohann,[4] Philippe Bendjoya,[9] Willy Benz,[7,21] Allyson Bieryla,[8] Xavier Bonfils,[22] François Bouchy,[23] Alexis Brandeker,[24] Christopher Broeg,[7,21] David J.A. Brown [1,2] Matthew R. Burleigh,[10] Marco Buttu,[25] Juan Cabrera,[26] Douglas A. Caldwell,[27] Sarah L. Casewell,[10] David Charbonneau,[8] Sébastian Charnoz,[28] Ryan Cloutier [8] Andrew Collier Cameron [3] Kevin I. Collins,[29] Dennis M.Conti,[30] Nicolas Crouzet,[31] Szilárd Czismadia [26] Melvyn B. Davies,[32] Magali Deleuil,[33] Elisa Delgado-Mena,[5] Laetitia Delrez [34,35] Olivier D. S. Demangeon,[5,6] Brice-Olivier Demory,[21] Georgina Dransfield [36] Xavier Dumusque,[23] Jo Ann Egger,[7] David Ehrenreich,[23] Philipp Eigmüller,[26] Anders Erickson,[26] Zahra Essack [37,38] Andrea Fortier,[7,21] Luca Fossati,[4] Malcolm Fridlund,[39,40] Maximilian N. Günther [31] Manuel Güdel,[41] Davide Gandolfi [42] Harvey Gillard,[1] Michaël Gillon,[34] Crystal Gnilka,[43,44] Michael R. Goad,[10] Robert F. Goeke,[38] Tristan Guillot,[9] Andreas Hadjigeorghiou,[1,2] Coel Hellier,[45] Beth A. Henderson,[10] Kevin Heng,[1,21] Matthew J. Hooton,[7,46] Keith Horne,[3] Steve B. Howell,[43] Sergio Hoyer [33] Jonathan M. Irwin,[8] James S. Jenkins [47,48] Jon M. Jenkins [43] Eric L. N. Jensen [49] Stephen R. Kane,[50] Alicia Kendall,[10] John F. Kielkopf,[51] Laszlo L. Kiss,[52,53] Gaia Lacedelli [54] Jacques Laskar,[55] David W. Latham,[8] Alain Lecavalier des Etangs,[56] Adrien Leleu,[7,23] Monika Lendl [23] Jorge Lillo-Box,[20] Christophe Lovis,[23] Djamel Mékarnia,[9] Bob Massey,[57] Tamzin Masters,[1] Pierre F. L. Maxted [45] Valerio Nascimbeni [54] Louise D. Nielsen,[58] Sean M. O'Brien,[59] Göran Olofsson,[24] Hugh P. Osborn [21,38] Isabella Pagano,[60] Enric Pallé,[12] Carina M. Persson,[61] Giampaolo Piotto,[54,62] Peter Plavchan [29] Don Pollacco,[1] Didier Queloz,[63,64] Roberto Ragazzoni,[54,62] Heike Rauer,[26,65,66] Ignasi Ribas,[15,16] George Ricker,[38] Damien Ségransan,[23] Sébastien Salmon,[23] Alexandre Santerne [33] Nuno C. Santos,[5,6] Gaetano Scandariato,[60] François-Xavier Schmider,[9] Richard P. Schwarz,[67] Sara Seager,[38] Avi Shporer,[38] Attila E. Simon,[7] Alexis M. S. Smith [26] Gregor Srdoc,[68] Manfred Steller,[4] Olga Suarez,[9] Gyula M. Szabó,[69,70] Johanna Teske,[71] Nicolas Thomas,[7] Rosanna H. Tilbrook [10] Amaury H. M. J. Triaud [36] Stéphane Udry,[23] Valérie Van Grootel,[34] Nicholas Walton,[72] Sharon X. Wang,[73] Peter J. Wheatley [1,2] Joshua N. Winn,[74] Robert A. Wittenmyer[11] and Hui Zhang[75]

Affiliations are listed at the end of the paper

Accepted 2023 January 26. Received 2022 August 10; in original form 2022 March 23

ABSTRACT

We present the discovery of two exoplanets transiting TOI-836 (TIC 440887364) using data from *TESS* Sector 11 and Sector 38. TOI-836 is a bright ($T = 8.5$ mag), high proper motion ($\sim$200 mas yr^{-1}), low metallicity ([Fe/H]≈-0.28) K-dwarf with a mass of 0.68 ± 0.05 M$_\odot$ and a radius of 0.67 ± 0.01 R$_\odot$. We obtain photometric follow-up observations with a variety of facilities, and we use these data sets to determine that the inner planet, TOI-836 b, is a 1.70 ± 0.07 R$_\oplus$ super-Earth in a 3.82-d orbit, placing it directly within the so-called 'radius valley'. The outer planet, TOI-836 c, is a 2.59 ± 0.09 R$_\oplus$ mini-Neptune in an 8.60-d orbit.

★ E-mail: faith.hawthorn@warwick.ac.uk (FH); d.bayliss@warwick.ac.uk (DB); tgw1@st-andrews.ac.uk (TW)

Radial velocity measurements reveal that TOI-836 b has a mass of $4.5 \pm 0.9\,M_\oplus$, while TOI-836 c has a mass of $9.6 \pm 2.6\,M_\oplus$. Photometric observations show Transit Timing Variations (TTVs) on the order of 20 min for TOI-836 c, although there are no detectable TTVs for TOI-836 b. The TTVs of planet TOI-836 c may be caused by an undetected exterior planet.

Key words: techniques: photometric – techniques: radial velocities – planets and satellites: detection – stars: individual: TOI-836 (TIC 440887364, GAIA EDR3 6230733559097425152).

1 INTRODUCTION

Since the groundbreaking discovery of 51 Pegasi b (Mayor & Queloz 1995), the field of exoplanet research has grown to now include an impressive 4935[1] discoveries using a variety of detection methods. Transit photometry and radial velocity spectroscopy continue to be the most fruitful methods of exoplanet discovery, and combined they also allow us to determine the fundamental properties of exoplanets, including their mass, radius, bulk density, and possible composition. Ground-based transit photometry surveys such as *HATNet* (Bakos et al. 2004), *WASP* (Pollacco et al. 2006), *KELT* (Pepper et al. 2007), *HAT-South* (Bakos et al. 2013), and *NGTS* (Wheatley et al. 2018) among others have greatly added to the population of known transiting exoplanets.

The advent of space-based transit surveys such as *CoRoT* (Auvergne et al. 2009), *Kepler* (Borucki et al. 2010), *K2* (Howell et al. 2014), and *TESS* (Ricker et al. 2015) has allowed us to extend the range of detectable exoplanets down to the regimes of Neptune and super-Earth radii. In this paper, we present the discovery of two such exoplanets found from *TESS* photometry to be transiting the bright star TOI-836. This system was included in the Magellan *PFS* survey paper (Teske et al. 2021).

The general conclusion from a number of studies is that *Kepler* compact planetary systems are flat, with the inclination dispersion on the order of a few degrees (Lissauer et al. 2011; Fang & Margot 2012; Figueira et al. 2012; Johansen et al. 2012; Tremaine & Dong 2012; Fabrycky et al. 2014). The discovery of such multiplanet systems (e.g. Wilson et al. 2022) confers significant advantages over those stars where only a single exoplanet is detected. First, the statistical likelihood that the transits are astrophysical false positives is greatly reduced (Lissauer et al. 2012). Secondly, the dynamical interactions between the planets can result in observable transit timing variations (TTVs), which in some cases may reveal the presence of non-transiting planets (e.g. Nesvorný et al. 2014). Thirdly, the comparative properties of the planets can reveal possible formation and migration pathways.

One particularly interesting aspect of small-radius multiplanet systems is looking at how they might allow us to study the origin and characteristics of the radius valley seen at around $R_p \approx 2.0\,R_\oplus$ in the exoplanet population (Owen & Wu 2013; Fulton et al. 2017). In the case of the TOI-836 system, we find that TOI-836 b lies within the radius valley itself, and TOI-836 c lies close to the peak on the right-hand side. The radius valley is valid for all systems, however multiplanet systems such as this may give us significant insights into formation mechanisms through comparative planetology.

This paper is structured as follows: we present our transit photometry, radial velocity, and imaging observations of the TOI-836 system in Section 2, our global modelling methods, associated computational implementations and results in Section 3. Finally we present our discussion and conclusion of these results in Sections 4 and 5, respectively.

[1]https://exoplanetarchive.ipac.caltech.edu as of 2022 February 22, (Akeson et al. 2013a)

Table 1. Catalogue stellar parameters of TOI-836.

Property	Value	Source
Identifiers		
TIC ID	TIC 440887364	TICv8
HIP ID	HIP 73427	–
2MASS ID	J15001942-2427147	*2MASS*
Gaia ID	6230733559097425152	*Gaia* EDR3
Astrometric properties		
R.A. (J2015.5)	$15^{h}00^{m}19\overset{s}{.}16$	*Gaia* EDR3
Dec (J2015.5)	$-24°27'15\overset{''}{.}14$	*Gaia* EDR3
Parallax (mas)	36.353 ± 0.016	*Gaia* EDR3
Distance (pc)	27.504 ± 0.029	–
$\mu_{\rm R.A.}$ (mas yr^{-1})	-199.48 ± 0.018	*Gaia* EDR3
$\mu_{\rm Dec}$ (mas yr^{-1})	-27.997 ± 0.017	*Gaia* EDR3
$\mu_{\rm Total}$ (mas yr^{-1})	201.438 ± 0.025	*Gaia* EDR3
$RV_{\rm sys}$ (km s^{-1})	-26.603 ± 0.922	*Gaia* DR2
Photometric properties		
TESS (mag)	8.649 ± 0.006	TICv8
B (mag)	11.138 ± 0.028	*APASS*
V (mag)	9.920 ± 0.030	*APASS*
G (mag)	9.407 ± 0.0003	*Gaia* EDR3
J (mag)	7.580 ± 0.023	*2MASS*
H (mag)	6.983 ± 0.040	*2MASS*
K (mag)	6.804 ± 0.018	*2MASS*
Gaia BP (mag)	10.126 ± 0.003	*Gaia* EDR3
Gaia RP (mag)	8.587 ± 0.004	*Gaia* EDR3

Note. Sources: TICv8 (Stassun et al. 2019), *2MASS* (Skrutskie et al. 2006), *Gaia* Early Data Release 3 (Gaia Collaboration 2021), *APASS* (Henden et al. 2016).

2 OBSERVATIONS

2.1 *TESS* discovery photometry

The transit signatures of TOI-836 b and TOI-836 c were originally identified by the *TESS* Science Processing Operations Center (Jenkins et al. 2016) using an adaptive matched filter (Jenkins 2002; Jenkins et al. 2010, 2020) to search the Sector 11 light curve on 2019 June 5. The transit signatures were fitted with an initial limb-darkened transit model (Li et al. 2019), and passed all the diagnostic tests performed and reported in the Data Validation reports (Twicken et al. 2018). The *TESS* Science Office reviewed the Data Validation reports and issued an alert for TOI-836 on 2019 June 17. Subsequent searches of the combined light curves from sectors 11 and 38 located the source of the transit events to within 3.73 ± 2.5 and 0.98 ± 1.5 arcsec of the host star for TOI-836 b and TOI-836 c, respectively. Note that the difference image centroiding results complement the high resolution imaging results presented in Section 2.5.

TOI-836 was first identified as a *TESS* Object of Interest (TOI; Guerrero et al. 2021) in *TESS* Sector 11, Camera 1, CCD 3 from 2019 April 22 to 2019 May 21. Stellar identifiers, astrometric properties, and photometric properties for TOI-836 are listed in Table 1. Fig. 1

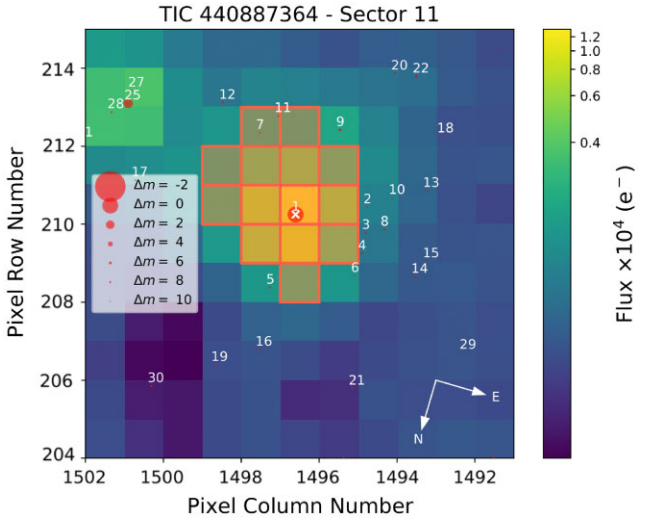

Figure 1. Target Pixel File (TPF) from *TESS* centred on TOI-836 from the *Gaia* catalogue, with *Gaia* DR2 sources indicated by red circles with scaled magnitudes, where the numbers indicate ranked distance from the target represented by a white cross. The aperture mask is outlined in red.

shows the Target Pixel File (TPF) from *TESS* created in `TPFPLOTTER`[2] (Aller et al. 2020), centred on TOI-836 (indicated by a white cross), with the *Gaia* DR2 catalogue data for sources overplotted in red along with scaled magnitudes and the aperture mask for photometry extraction.

TOI-836 showed transit events from two exoplanet candidates, designated TOI-836.01 (TOI-836 c; SNR = 21) and TOI-836.02 (TOI-836 b; SNR = 17), identified from the *TESS* light curves. In Sector 11, TOI-836 b shows five transit events and one partial (egress only) transit, while TOI-836 c shows two transit events. One transit event of TOI-836 b would have occurred in the gap during which the satellite downloads data. See Table 2 and the left-hand panel of Fig. 2.

TOI-836 was observed again in the third year of *TESS* operations during Sector 38, Camera 1, CCD 4 from 2021 April 28 to 2021 May 26. Seven transit events were observed for TOI-836 b, and three for TOI-836 c. See Table 2 and right-hand panel of Fig. 2.

The transits of TOI-836 b indicate an orbital period of 3.82 d. The transit depth was 580 ppm, implying the planet candidate is a potential hot super-Earth. For TOI-836 c the orbital period is 8.60 d, and the transit depth is 1140 ppm, implying the candidate is potentially sub-Neptune in size.

For this work, we use the Presearch Data Conditioning Simple Aperture Photometry (PDC-SAP) light curve produced by the SPOC pipeline. The PDC-SAP light curves have non-astrophysical trends removed from the raw Simple Aperture Photometry (SAP) light curves using the PDC algorithm (Smith et al. 2012; Stumpe et al. 2012, 2014). The PDC-SAP light curves for TOI-836 were retrieved from the Mikulski Archive for Space Telescopes (MAST) portal and used in our joint model in Section 3.

To mitigate for the effects of stellar variability on the transit light curves in the Sector 11 and Sector 38 *TESS* data, we apply a Gaussian Process (GP) model using the `PyMC3` and `celerite` packages. We constrain this GP model for each sector using three hyperparameters as priors set up with log(*s2*) (a jitter term describing the excess white noise; Salvatier, Wiecki & Fonnesbeck 2016) and log(*Sw4*) as normal distributions with a mean equal to the variance of the flux of each sector and a standard deviation of 0.1 for Sector 11 and 0.05 for Sector 38 (this is done to prevent overfitting of the GP); and the same is applied to log(*w0*). log(*Sw4*) and log(*w0*) both represent terms that describe the non-periodic variability of the light curves (Salvatier et al. 2016). These hyperparameter setups are identical to those described for TOI-431 in Osborn et al. (2021) and informed by the `exoplanet` and `PyMC3` documentation. These hyperparameters are then incorporated into the SHOTerm kernel within the `exoplanet` framework, representing a stochastically driven simple harmonic oscillator (Foreman-Mackey et al. 2021a). The GP model is then subtracted from the PDC-SAP flux to recover a flattened light curve from which transit models of TOI-836 b and TOI-836 c can be drawn. The effect of this can be seen in the first and second panels of Fig. 2 for Sector 11 and Sector 38 of *TESS*, respectively. We also plot the phase-folded *TESS* data for TOI-836 b and TOI-836 c in Fig. 3 for both sectors.

For all follow-up photometry, we convert each time system to TBJD (*TESS* Barycentric Julian Date, BJD-2457000) for consistency, and normalize each light curve by dividing by the median of the out-of-transit flux data points and subtracting the mean of the out-of-transit flux. The transits themselves are then modelled using a quadratic limb-darkened Keplerian orbit (with coefficients u_1 and u_2) according to Kipping (2013b), with parameters including stellar radius (R_*) and mass (M_*) in Solar units, planetary orbital period (P) in days, transit ephemeris (T_c) in TBJD, impact parameter (b), eccentricity (e), and argument of periastron (ω) defined for each of TOI-836 b and TOI-836 c with priors informed by our spectral analysis and catalogue data (see Appendix Tables A1, A2, and A3 for details of the priors used). Transit models for each set of photometry time-series data are then created using the `starry` package within `exoplanet`, along with their corresponding planetary radii (R_p), time of the data (t) and exposure times for each instrument t_{exp}.

2.2 CHEOPS photometry

The transit depths for TOI-836 b and TOI-836 c are 580 ppm and 1140 ppm, respectively, making them challenging for photometric follow-up efforts. The *CHEOPS* mission is able to reach a precision of 15 ppm per 6 h for a star with $V = 9$ mag (Benz et al. 2021), and *CHEOPS* is therefore in a unique position to confirm and characterize shallow transit discoveries from *TESS*, as has been shown in recent publications (Bonfanti et al. 2021; Delrez et al. 2021; Leleu et al. 2021).

In order to better determine the planet radii and orbital ephemerides, and check for any TTVs, we observed TOI-836 with *CHEOPS* spacecraft between 2020 May 25 and 2021 May 4, as a part of the Guaranteed Time Observing program, yielding a total of 57.81 h on target. Five observations of TOI-836 were taken by the *CHEOPS* satellite, resulting in the recovery of four transits of TOI-836 c, and one transit of TOI-836 b. For all visits, we use an exposure time of 60 s. See details set out in Table 2.

The *CHEOPS* spacecraft is in a low-Earth orbit and thus parts of the observations are unobtainable because the telescope passes through the South Atlantic Anomaly (SAA), and as the amount of stray-light entering the telescope becomes higher than the accepted threshold, our observations are interrupted by Earth occultations. These effects that occur on orbital time-scales (~98.77 min) result in onboard rejections of images and manifest in a decrease in

[2]https://github.com/jlillo/tpfplotter

Table 2. Photometric observations of TOI-836.

Instrument	Aperture	Filter	Exposure time (s)	No. of images	UT night	Planet	Epoch no.
TESS	0.105 m	*TESS*[1]	120	19527	2019 Apr	TOI-836 b	Epochs 1–7
					22–2019 May 20	TOI-836 c	Epochs 1–2
MEarth-South	0.4 m × 7	RG715	32	3054	2019 Jul 4	TOI-836 c	Epoch 8
LCOGT-SSO	1.0 m	*Y*	40	232	2020 Feb 29	TOI-836 c	Epoch 36
LCOGT-CTIO[A]	1.0 m	*Y*	100	138	2020 Mar 8	TOI-836 b	Epoch 83
LCOGT-SSO[B]	1.0 m	*Y*	100	109	2020 Mar 20	TOI-836 b	Epoch 86
LCOGT-SSO	1.0 m	z_s	30	341	2020 Apr 12	TOI-836 c	Epoch 41
LCOGT-SSO	1.0 m	*Y*	100	260	2020 May 4	TOI-836 b	Epoch 98
LCOGT-SAAO[C]	1.0 m	z_s	30	327	2020 May 16	TOI-836 c	Epoch 45
CHEOPS	0.32 m	*CHEOPS*[2]	60	398	2020 May 25	TOI-836 c	Epoch 46
CHEOPS	0.32 m	*CHEOPS*[2]	60	319	2020 Jun 28	TOI-836 c	Epoch 50
CHEOPS	0.32 m	*CHEOPS*[2]	60	318	2020 Jul 7	TOI-836 c	Epoch 51
CHEOPS	0.32 m	*CHEOPS*[2]	60	574	2020 Jul 8	TOI-836 b	Epoch 115
LCOGT-SSO	1.0 m	z_s	30	345	2021 Apr 8	TOI-836 c	Epoch 83
ASTEP	0.4 m	R_c	25	370	2021 Apr 8	TOI-836 c (egress)	Epoch 83
NGTS	0.2 m × 3	*NGTS*[3]	10	5405	2021 Apr 16	TOI-836 c	Epoch 84
LCOGT-CTIO	1.0 m	z_s	30	382	2021 Apr 16	TOI-836 c	Epoch 84
TESS	0.105 m	*TESS*[1]	120	19226	2021 Apr	TOI-836 b	Epochs 194-
					29–2021 May 26	TOI-836 c	200 Epochs 86-88
CHEOPS	0.32 m	*CHEOPS*[2]	60	431	2021 May 4	TOI-836 c	Epoch 86
LCOGT-CTIO	1.0 m	z_s	30	300	2021 Jun 24	TOI-836 c	Epoch 92

Notes.[1] *TESS* custom 600–1000 nm [2]*CHEOPS* custom 350–1100 nm [3]*NGTS* custom 520–890 nm
[A]CTIO – Cerro Tololo Inter-American Observatory [B]SSO – Siding Spring Observatory [C]SAAO – South Africa Astronomical Observatory.

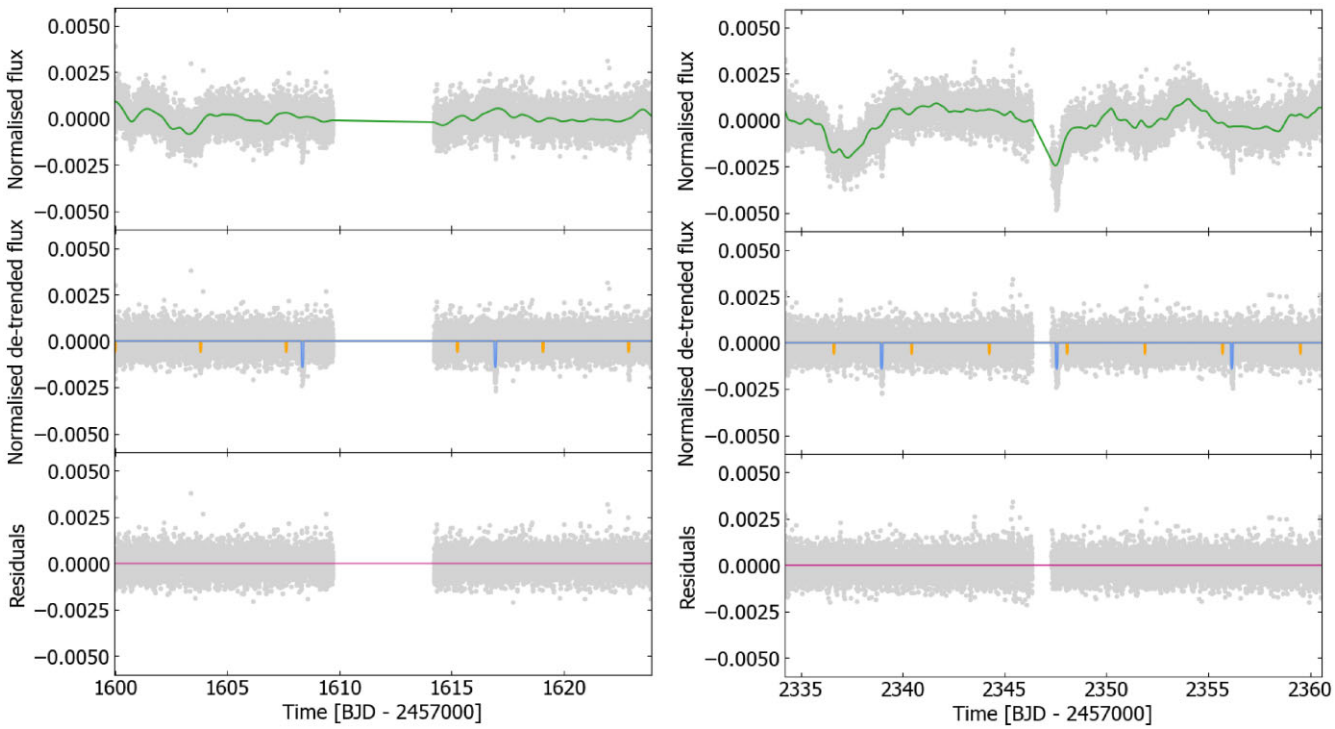

Figure 2. Top left-hand panel: *TESS* PDC-SAP light curve from Sector 11 with the GP model plotted in green. Middle left-hand panel: *TESS* PDC-SAP light-curve data minus the GP model, with transits plotted for TOI-836 c (blue line) and TOI-836 b (orange line). Bottom left-hand panel: Residuals between the best-fitting model and the *TESS* data points. Top right-hand panel: *TESS* PDC-SAP light curve from Sector 38 with the GP model plotted in green. Middle right-hand panel: *TESS* PDC-SAP light-curve data minus the GP model, with transits plotted for TOI-836 c (blue line) and TOI-836 b (orange line). Bottom right-hand panel: Residuals between the best-fitting model and the *TESS* data points.

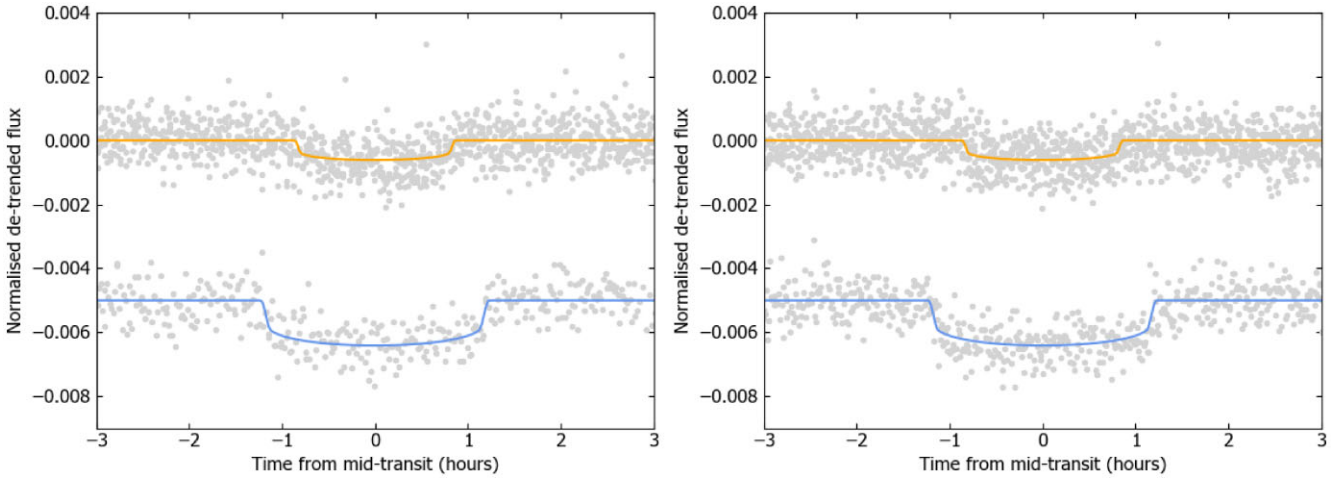

Figure 3. Left-hand panel: *TESS* PDC-SAP light curve from Sector 11 minus the GP model, phase-folded to a period corresponding to that of TOI-836 b with the transit model shown in orange and phase-folded to a period corresponding to that of TOI-836 c with the transit model shown in blue. The data for TOI-836 c has been offset by −0.005 for clarity. Right-hand panel: *TESS* PDC-SAP light curve from Sector 38 minus the GP model, phase folded and offset for each planet analogously to that of Sector 11.

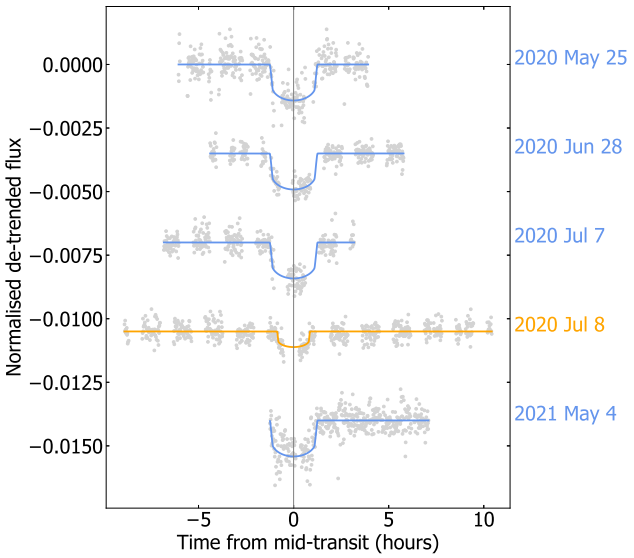

Figure 4. Light curves of TOI-836 b and TOI-836 c taken by the *CHEOPS* satellite as detailed in Table 2, plotted with our best-fitting `exoplanet` models for TOI-836 b in orange and TOI-836 c in blue, and offset for clarity.

observational efficiency, corresponding to 72 per cent, 55 per cent, 56 per cent, 54 per cent, and 96 per cent per visit, as can be seen in Fig. 4.

For all visits, the data were automatically processed using the *CHEOPS* data reduction pipeline (DRP v13; Hoyer et al. 2020), that conducts image calibration, such as bias, gain, non-linearity, dark current, and flat fielding corrections, and performs rectifications of environmental and instrumental effects, for example cosmic-ray hits, smearing trails, and background variations. Aperture photometry is subsequently done on the corrected images using a set of standard apertures; R = 22.5 arcsec (RINF), 25.0 arcsec (DEFAULT), and 30.0 arcsec (RSUP), and an additional aperture that aims to optimize the radius based on contamination level and instrumental noise (ROPT). For the *CHEOPS* observations of TOI-836, this radius is either 29.0 or 29.5 arcsec. The DRP also computes a contamination estimate of background sources, as detailed in section 6.1 of Hoyer et al. (2020), that is subtracted from the light curves.

Due to the orbit of *CHEOPS* and thus the rotating field of view, *CHEOPS* data include short-term, non-astrophysical flux trends due to nearby contaminants, background variations, or changes in instrumental environment that vary on the time-scale of the orbit of *CHEOPS*. Whilst previous works have used linear decorrelation with instrumental basis vectors (Bonfanti et al. 2021; Delrez et al. 2021; Leleu et al. 2021) or Gaussian process regression (Lendl et al. 2020), a recent study has shown that a novel PSF detrending method can also remove these roll angle trends (Wilson et al. 2022). In brief, this method assesses PSF shape changes over a visit by conducting a principal component analysis on the autocorrelation function of the *CHEOPS* subarray images, as it was found that a myriad of causes of systematic variation within *CHEOPS* data affects the PSF shape. A leave-one-out-cross-validation (Celisse 2008) is used to select the most prominent components that are subsequently used to decorrelate the light curve produced by aperture photometry. We apply this method to the TOI-836 *CHEOPS* observations with fluxes obtained with the DEFAULT aperture. The decorrelated CHEOPS data are presented in Table 3, along with the resulting light curves in Fig. 4.

Table 3. *CHEOPS* photometric data for TOI-836. This table is available in its entirety online.

Time (BJD -2457000)	Normalized flux	Flux uncertainty
1994.88704	0.99981	0.00025
1994.88773	0.99955	0.00026
1994.88843	1.00105	0.00027
1994.88912	1.00140	0.00030
1994.88982	1.00033	0.00035
1994.90649	0.99897	0.00027
1994.90718	0.99896	0.00026
1994.90788	1.00011	0.00025
1994.90857	1.00045	0.00025
...	...	...

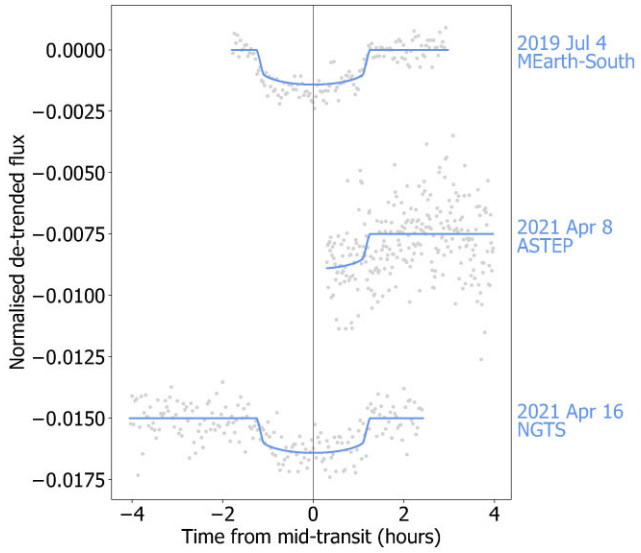

Figure 5. Light curves of TOI-836 c taken by the *MEarth-South*, *NGTS*, and *ASTEP* facilities as detailed in Table 2, plotted with our best-fitting `exoplanet` models and offset for clarity.

2.3 Ground-based follow-up photometry

2.3.1 MEarth-South photometry

A transit of TOI-836 c was observed using the *MEarth-South* telescope array (Irwin et al. 2015a) at Cerro Tololo Inter-American Observatory (CTIO), Chile on 2019 July 3–4. Seven telescopes were operated defocused to a half-flux diameter of 12 pixels (10.1 arcsec, given the pixel scale of 0.84 arcsec pix^{-1}), and an exposure time of 32 s, observing continuously starting from twilight until the target set below 2 airmasses. Observations were made using an RG715 filter. A meridian flip occurred during the transit and has been taken into account in the analysis by allowing for a separate magnitude zero-point on either side of the meridian to remove any residual flat fielding error.

Data were reduced following standard procedures for *MEarth-South* data (e.g. Irwin et al. 2007, 2015a) with a photometric extraction aperture of radius 17 pixels (14.3 arcsec). To account for residual colour-dependent atmospheric extinction the transit model included linear decorrelation against airmass. The edge of the photometric aperture is slightly contaminated by fainter sources, the most significant being TIC 440887361, but we estimate that this source is approximately 10.6 *TESS* magnitudes fainter than the target star, so the resulting dilution of the measured transit depth should be negligible. The *MEarth-South* light curve is shown in Fig. 5 and used in the joint modelling in Section 3.2.

2.3.2 ASTEP photometry

ASTEP (Antarctic Search for Transiting ExoPlanets) is a 40 cm Newtonian telescope designed to perform high precision photometry under the extreme conditions of the Antarctic winter (Fressin et al. 2005; Daban et al. 2010; Abe et al. 2013; Guillot et al. 2015; Mékarnia et al. 2016). It is installed at the French-Italian Concordia station at Dome C, Antarctica (75° 06' S, 123° 21' E) on a summit of the high Antarctic plateau, at an altitude of 3233 m, 1100 km inland. Dome C is an ideal location for time-series observations thanks to the 4-month continuous night during the Antarctic winter and favourable weather conditions (Crouzet et al. 2010, 2018). *ASTEP* is equipped with a FLI Proline KAF 16801 E 4096 × 4096 pixel CCD camera observing in an R_c band-pass, the field of view is 1° × 1° and the pixel size is 0.9 arcsec pixel^{-1}.

We observed TOI-836 on 2021 April 8, during 5 h between BJD 2459313.20 and 2459313.41, and we detected the second half of the transit of TOI-836 c. We scheduled the observation using a custom scheduling tool that sends queries to the `TESS Transit Finder`. We set the exposure time to 25 s, the cadence was 50 s, and we collected 370 frames. The median full-width half maximum (FWHM) was 4.06 arcsec and the airmass varied between 1.57 and 1.94. The details of the *ASTEP* observations are set out in Table 2. We performed differential aperture photometry using a custom data reduction pipeline based on the pipeline described in Mékarnia et al. (2016) and adapted to *TESS* follow-up. We used an aperture radius of 10 pixels (9.3 arcsec) and 8 comparison stars. The light curve RMS is 1.43 ppt and decreases to 1.2 ppt after binning the light curve with a bin size of 3 points, for a predicted transit depth of 1.38 ppt. The transit appears clearly and is on target. The *ASTEP* light curve is shown in Fig. 5 and used in the joint modelling in Section 3.2. The *ASTEP* telescope is now being upgraded with two new cameras that will observe simultaneously in two colours and will provide a much better throughput (Crouzet et al. 2020).

2.3.3 NGTS photometry

We monitored a full transit of TOI-836 c on the night of 2021 April 16 using three of the *NGTS* (Next Generation Transit Survey; Wheatley et al. 2018) telescopes at the ESO Paranal Observatory, Chile. The observations were performed using the *NGTS* multitelescope observing method described in Bryant et al. (2020) and Smith et al. (2020). *NGTS* consists of an array of 0.2 m robotic telescopes, each with a wide field-of-view of 8 deg^2. A custom *NGTS* filter of 520–890 nm is used, and images are taken using Andor iKon-L 936 cameras, which deliver a plate-scale of 5 arcsec pix^{-1}. We use an exposure time of 10 s, and with readout time this translates to a cadence of approximately 13 s. The details of the *NGTS* observations are set out in Table 2.

The *NGTS* image reduction was performed using an adapted version of the standard *NGTS* pipeline (Wheatley et al. 2018), which has been updated to perform aperture photometry for a single star. Comparison stars which are isolated and similar to TOI-836 in brightness and CCD position were automatically identified by the pipeline using *Gaia* DR2 (Gaia Collaboration 2018). The resultant flux from each telescope was detrended independently against airmass, and the photometry from the three telescopes is combined into a single light-curve file, which is publicly available from the ExoFOP-TESS website.[3] The *NGTS* light curve is shown in Fig. 5 and used in the joint modelling in Section 3.2.

2.3.4 LCO photometry

We observed three full transits of TOI-836 b and six full transits of TOI-836 c from the Las Cumbres Observatory Global Telescope (*LCOGT*; Brown et al. 2013) 1.0 m network. The details of the *LCOGT* observations are set out in Table 2. We used the `TESS Transit Finder`, which is a customized version of the `Tapir` software package (Jensen 2013), to schedule our transit observations. The telescopes are equipped with 4096 × 4096 SINISTRO cameras

[3] https://exofop.ipac.caltech.edu/tess/

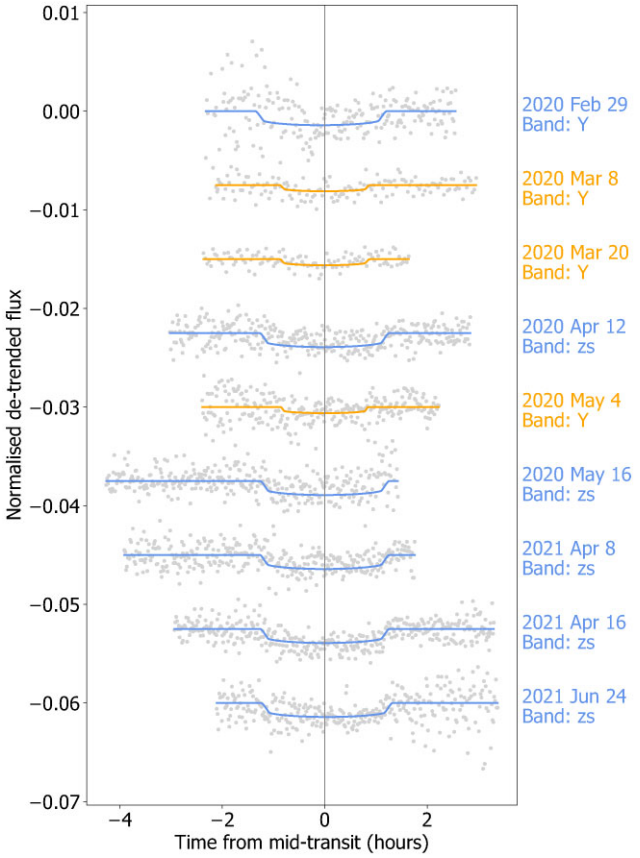

Figure 6. Light curves of TOI-836 b and TOI-836 c taken by the *LCOGT* network as detailed in Table 2, plotted with our best-fitting `exoplanet` models for TOI-836 b in orange and TOI-836 c in blue, and offset for clarity.

having an image scale of 0.389 arcsec per pixel, resulting in a 26 arcmin × 26 arcmin field of view. The images were calibrated by the standard *LCOGT* `BANZAI` pipeline (McCully et al. 2018), and photometric data were extracted using `AstroImageJ` (Collins et al. 2017). The *LCOGT* light curves are shown in Fig. 6 for TOI-836 b and TOI-836 c, and used in the joint modelling in Section 3.2.

2.3.5 *WASP-South photometry*

The *WASP-South* array of eight wide-field cameras was the Southern station of the *WASP* transit-search project (Pollacco et al. 2006). *WASP-South* observed the field of TOI-836 repeatedly over the years 2006 to 2014, observing with a broad-band filter, and accumulating a total of 93 000 photometric data points. While the precision of these observations is not sufficient to detect the transits, the long-duration monitoring is ideal for detecting photometric activity due to star spots. We thus searched the data for a rotational modulation using the methods discussed in Maxted et al. (2011). We find a persistent periodicity with a period of 22.0 ± 0.1 d, where the uncertainty estimate makes allowance for phase changes caused by changing star-spot patterns. The amplitude varies from 3 to 8 mmag and the false-alarm probability in each season's data set is typically < 1 per cent. In Fig. 7 we show periodograms from two seasons of data, together with the resulting modulation profile from folding the data.

The 22-d period is consistent with activity seen in the *TESS* data, particularly in Sector 38 data (see Fig. 2). We therefore adopt this

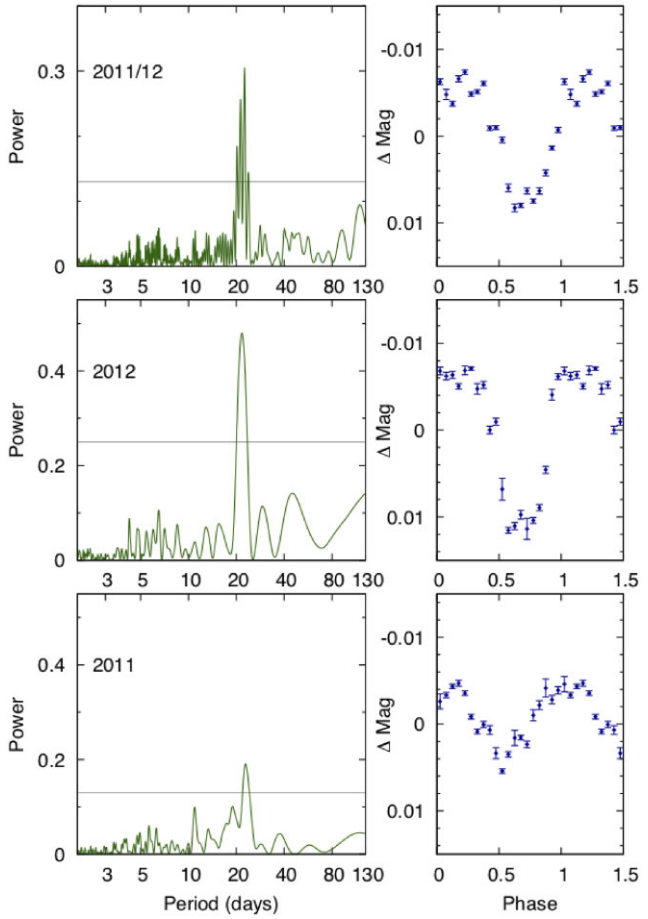

Figure 7. Left-hand panels: Periodograms of the *WASP-South* lightcurves of TOI-836 from 2011 and 2012, and for 2011 and 2012 combined. The horizontal line is the estimated 1 per cent-likelihood false-alarm level. Right-hand panels: *WASP-South* photometry data, phase-folded to the best stellar rotation period estimate.

as the likely spin period of the star and use it to inform our joint modelling in Section 3.2.

2.4 Follow-up spectroscopy

In order to determine the stellar parameters and measure radial velocity variations, a number of spectrographs were used to observe TOI-836. Two reconnaissance spectra were taken on 2019 July 1 and 2021 May 28 with the Tillinghast Reflector Echelle Spectrograph (*TRES*) (Fűrész 2008) on the 1.5 m telescope at the Fred Lawrence Whipple Observatory (FLWO). The spectra were used to derive stellar parameters using the Stellar Parameter Classification (SPC) tool (Buchhave et al. 2012; Buchhave et al. 2014). These spectra indicated that TOI-836 is a K-dwarf with a low $v \sin i_*$ that would be amenable to high-precision radial velocity follow-up. In this section, we describe these high-precision radial velocity data, which are obtained using the *HARPS* and *PFS* spectrographs. We also obtain 11 spectra from the *HIRES* spectrograph (Vogt & Penrod 1988), taken from 2009 April 6 to 2013 February 3, which we use to examine long-term radial velocity trends. The iSHELL radial velocities were taken at 2.3 microns, and as we do not implement a chromatic RV analysis as in Cale et al. (2021), we exclude them from our analysis. Additional radial velocity data from *MINERVA-Australis* also exist,

Table 4. *HARPS* spectroscopic data for TOI-836. This table is available in its entirety online.

Time (BJD -2457000)	RV ($m\,s^{-1}$)	RV error ($m\,s^{-1}$)	FWHM ($m\,s^{-1}$)	Bisector ($m\,s^{-1}$)	Contrast	S-index$_{MW}$
1924.744232	−26270.62	1.20	6479.82	59.29	42.086199	1.118916
1924.847515	−26272.89	1.13	6477.87	58.02	42.082108	1.088405
1925.765286	−26277.15	1.33	6483.37	54.98	42.104065	1.099795
1925.897310	−26278.60	1.42	6484.65	62.33	42.063377	1.035016
1926.748165	−26279.33	1.23	6481.65	63.03	42.111069	1.073716
1926.891093	−26276.88	1.25	6474.28	65.77	42.150971	1.039492
1927.807982	−26280.90	1.66	6472.36	61.35	42.201152	1.068344
1927.885303	−26283.22	1.24	6470.19	62.19	42.177954	1.035070
1928.764641	−26288.22	1.24	6465.28	65.38	42.164275	1.058810
1928.890901	−26289.86	1.37	6466.36	65.65	42.174431	1.042093
...	...	...	...	...	...	...

Table 5. Radial velocity follow-up details for TOI-836. Observations used in the joint model are marked with an asterisk.

Facility	Telescope aperture	No. of spectra	Resolution
HARPS ∗	3.6 m	52	115 000
HIRES	10.0 m	11	60 000
PFS ∗	6.5 m	30	130 000
iSHELL	3.0 m	10	70 000
MINERVA-Australis	0.7 m × 6	27	75 000

Note. Sources: *HARPS* (Mayor et al. 2003), *HIRES* (Vogt & Penrod 1988), *PFS* (Crane, Shectman & Butler 2006), *iSHELL* (Rayner et al. 2012), *MINERVA-Australis* (Wittenmyer et al. 2018; Addison et al. 2019, 2021)

but the lower precision of these data mean that we omit them from our analysis.

2.4.1 *HARPS* radial velocity observations

HARPS (High Accuracy Radial velocity Planet Searcher; Mayor et al. 2003) is an Echelle spectrograph mounted on the ESO 3.6 m telescope situated at La Silla Observatory, Chile. A total of 52 spectra of TOI-836 were obtained with *HARPS* as part of the *NCORES* program (PI D. Armstrong, 1102.C-0249). 15 of these spectra were obtained from 2020 March 16 to 2020 March 23 (7 nights), followed by a further 37 spectra from 2021 January 22 to 2021 March 2 (39 nights). These data were obtained in *HARPS* High-Accuracy Mode with a 1 arcsec diameter fibre, standard resolution of $R\sim$115 000, and exposure times of approximately 1500 s. Raw data were reduced according to the standard *HARPS* data reduction software detailed in Lovis & Pepe (2007). The data table for these observations can be found in Table 4, which we use in our joint modelling (Section 3.2). The *HARPS* data are marked with an asterisk in Table 5.

2.4.2 *PFS* radial velocity observations

The Planet Finder Spectrograph (PFS) (Crane et al. 2006; Crane et al. 2008, 2010) is a high resolution optical Echelle spectrograph mounted on the 6.5 m Magellan II Telescope at Las Campanas Observatory, Chile. PFS is calibrated via an iodine-cell, and raw data are reduced to 1D spectra and relative radial velocities extracted using a custom pipeline based on Butler et al. (1996). The spectrograph was upgraded in 2018, and now operates with a default slit width of 0.3 arcsec, which delivers a resolving power of $R\sim$130 000.

TOI-836 was observed as part of the Magellan-*TESS* Survey (Teske et al. 2021) between 2019 July 10 to 2020 March 17. Exposure times were approximately 900–1200 s per individual observation, and usually two observations were taken per night (separated by ∼2 h) and binned together. In total, 38 binned radial velocities were published in Teske et al. for TOI-836, and these are set out in table 4 of Teske et al. (2021). We use the PFS radial velocities in our joint modelling (Section 3.2). The PFS data are marked with an asterisk in Table 5.

2.4.3 *HIRES* radial velocity observations

HIRES (High Resolution Echelle Spectrometer; Vogt & Penrod 1988) is an $R\sim$60 000 resolving power spectrograph mounted on the 10 m Keck Telescope at Mauna Kea Observatory, Hawaii. Like *PFS*, *HIRES* also operates with an iodine-cell wavelength calibration, and data are reduced using a custom pipeline based on Butler et al. (1996).

TOI-836 was observed as part of the Lick-Carnegie Exoplanet Survey (Butler et al. 2017) between 2009 April 6 to 2013 February 3. In total, 11 observations were made over this four year time period, with a typical exposure time of approximately 500 s. These data are set out in table 1 of Butler et al. (2017). The observations were made prior to the discovery of the transiting planets TOI-836 b and TOI-836 c. The low cadence of these observations, coupled with the stellar activity of TOI-836, means that we decided not to use them in our GP-based joint model of Section 3.2 – however they do enable us to study any long-term radial velocity trends for the system (see Section 3.2.4).

2.5 Imaging

The large size of the *TESS* pixels (21 arcsec) necessitates a careful study of neighbouring regions in order to determine if there are stars blended in to the *TESS* photometric data. In such cases, planet transits can be mimicked by other stellar configurations (e.g. Howell et al. 2011; Lillo-Box, Barrado & Bouy 2012; Lillo-Box, Barrado & Bouy 2014; Furlan et al. 2017). *Gaia* shows TOI-836 to be a relatively isolated star, with no neighbours with $\Delta\, T_{\rm mag} < 6$ in the photometric aperture to within its sensitivity limits (see Fig. 1). To probe regions very close to TOI-836 (< 1.5 arcsec), where *Gaia* is known to be incomplete, we use direct imaging from large ground-based telescopes.

TOI-836 was imaged by multiple telescopes and instruments in order to check for close companions. This imaging includes *Gemini*-Zorro and *Gemini*-'Alopeke (Scott et al. 2021), *VLT*-NaCo (Rousset et al. 2003), *Keck*-2-NIRC2 (Ciardi et al. 2015), and *SOAR*-HRCam (Ziegler et al. 2020). These imaging data are publicly available

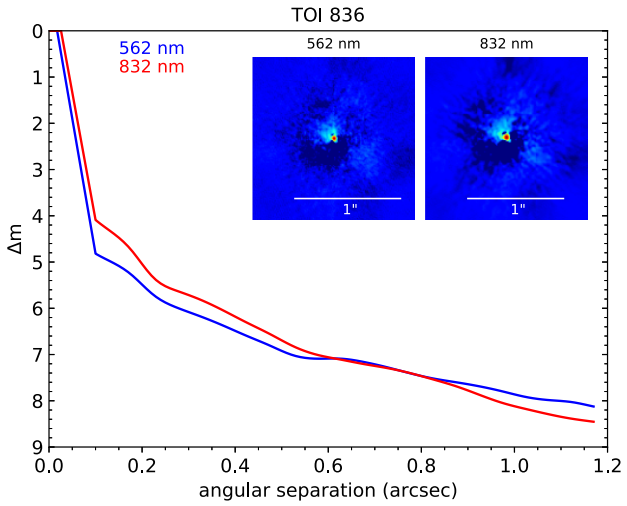

Figure 8. Reconstructed images and speckle sensitivity curves of TOI-836 taken on 2020 March 13 using Zorro on the *Gemini*-South 8.0 m telescope at Cerro Pachón, Chile, in each of the two bandpasses. No close companions are visible brighter than a contrast of 5 mag for separations between 0.2 and 1.2 arcsec. Other direct imaging data also place similar constraints on the presence of close companions.

from the ExoFOP-TESS website.[4] The conclusion from all of these imaging data is that TOI-836 has no close companions outside a separation of 0.2 arcsec.

As an example of this direct imaging data, Fig. 8 shows the reconstructed images and speckle sensitivity curves from the observation taken using the Zorro instrument (Scott et al. 2021) on *Gemini*-South at Cerro Pachón Observatory, Chile. This imaging was taken on 2020 March 13 in two simultaneous passbands (562 and 832 nm), and like all the direct imaging, shows that TOI-836 is an isolated star to within the 5 σ contrast limits.

3 METHODS AND RESULTS

3.1 Stellar analysis

To determine the stellar parameters for TOI-836, we co-add the 52 *HARPS* spectra (Section 2.4.1) into a single combined spectrum with a signal-to-noise of ∼400 at 550 nm. We use the method described in Sousa (2014) and Santos et al. (2013) in order to derive the stellar atmospheric parameters including a trigonometric surface gravity $\log g$, effective temperature $T_{\rm eff}$, and metallicity [Fe/H]. This method measures the equivalent widths of iron lines in the combined *HARPS* spectrum via the `ARES` v2 code (Sousa et al. 2015). The abundances are then estimated using the `MOOG` code (Sneden 1973) for radiative transfer, which includes a grid of model atmospheres from Kurucz (1993), and we find the best set of spectroscopic parameters by assuming equilibriums of ionization and excitation. Following the same methodology as described in Sousa et al. (2021), we use the *Gaia* EDR3 parallax and estimate the trigonometric surface gravity. This spectral analysis shows that TOI-836 is a K-dwarf with a $\log g = 4.743 \pm 0.105$ dex and a $T_{\rm eff} = 4552 \pm 154$ K. We find a metallicity of [Fe/H] $= -0.284 \pm -0.067$ dex and a $v \sin i_* = 1.86 \pm 0.50\,{\rm km\,s^{-1}}$.

[4] https://exofop.ipac.caltech.edu/tess/

To obtain the radius of TOI-836, we use a Markov–Chain Monte Carlo (MCMC) modified infrared flux method (IRFM; Blackwell & Shallis 1977; Schanche et al. 2020). This is done by building spectral energy distributions (SEDs) from Atlas Catalogue stellar atmospheric models (Castelli & Kurucz 2003) and stellar parameters derived via our spectral analysis, and calculating synthetic fluxes by integrating the SEDs over bandpasses of interest after attenuation to account for extinction. These fluxes are compared to observed broadband photometry retrieved from the most recent data releases for the following bandpasses; *Gaia* G, G_{BP}, and G_{RP} (Gaia Collaboration 2021), 2MASS J, H, and K (Skrutskie et al. 2006), and *WISE W1* and *W2* (Wright et al. 2010) to calculate the apparent bolometric flux, and hence the stellar angular diameter and effective temperature. By converting the angular diameter to the stellar radius using the offset-corrected *Gaia* EDR3 parallax (Lindegren et al. 2021), we obtain $R_* = 0.666 \pm 0.010\,{\rm R}_\odot$.

Starting from the basic input set given by ($T_{\rm eff}$, [Fe/H], R_*), we then derived the isochronal mass M_* and age t_*. To provide robust estimates, we employed two different evolutionary models, namely `PARSEC`[5] v1.2S (Marigo et al. 2017) and `CLES` (Code Liègeois d'Évolution Stellaire, Scuflaire et al. 2008). In detail, we derived a first pair of mass and age values using the isochrone placement technique (Bonfanti et al. 2015; Bonfanti, Ortolani & Nascimbeni 2016), which we applied to pre-computed tables of `PARSEC` tracks and isochrones. Besides the basic input set, we further inputted the $v \sin i_*$ value to improve the convergence of the interpolating routine as detailed in Bonfanti et al. (2016). A second pair of mass and age estimates was instead retrieved through the `CLES` code, which generates the best stellar evolutionary track that reproduces the basic input set following the Levenberg-Marquadt minimization scheme (Salmon et al. 2021). After carefully checking the mutual consistency of the two respective pairs of values through the χ^2-based criterion outlined in Bonfanti et al. (2021), we finally merged the two output mass and age distributions and we obtained $M_* = 0.678^{+0.049}_{-0.041}\,{\rm M}_\odot$ and $t_* = 5.4^{+6.3}_{-5.0}$ Gyr. We use these values of the stellar mass and radius as priors within our `exoplanet` modelling (described in Section 3.2), which are then fit for in the code to produce the final values seen in Table 6.

Further to this, we derive stellar abundances using the curve-of-growth analysis method in local thermodynamic equilibrium, as employed in Adibekyan et al. (2012, 2015). We are unable to derive reliable values for the abundances of C and O because the lines for those elements become very weak and blended with other species for cool dwarf stars, as it is in the case of TOI-836 (see e.g. Delgado Mena et al. 2021). The values of [Mg/H] and [Si/H] are -0.23 ± 0.17 and -0.29 ± 0.20 dex, respectively. These are typical values for a thin-disc star, which agrees with our calculated Galactic space velocity components and thin-disc membership probability as described in the next paragraph. There is no evidence in the stellar spectrum (such as a strong Li line) to suggest that TOI-836 is a young star. The full set of results from our spectral analysis are set out in Table 6.

Following the formulation of Johnson & Soderblom (1987), and using the values of proper motion and parallax from *Gaia* EDR3 (see Table 1), and a radial velocity from *Gaia* DR2 of $-26.603 \pm 0.922\,{\rm km\,s^{-1}}$ (Gaia Collaboration 2018), we calculate the values and uncertainties for U, V, and W, the heliocentric velocity components of the Galactic space velocities, in the direction of the galactic centre, rotation, and pole, respectively, in Table 6. We should

[5] *PA*dova and T*R*ieste *S*tellar *E*volutionary *C*ode: http://stev.oapd.inaf.it/cgi-bin/cmd

Table 6. Stellar parameters of TOI-836.

Property (unit)	Value	Source
Mass ($M_\odot$)	$0.678^{+0.049}_{-0.041}$	`exoplanet`
Radius ($R_\odot$)	0.665 ± 0.010	`exoplanet`
Density (g cm^{-3})	$3.294^{+0.079}_{-0.092}$	`exoplanet`
$P_{\rm rot}$ (d)	21.987 ± 0.097	`exoplanet`
LD coefficient u_1	0.039 ± 0.235	`exoplanet`
LD coefficient u_2	0.023 ± 0.335	`exoplanet`
log g	4.743 ± 0.105	`ARES` + `MOOG` + *Gaia*
$T_{\rm eff}$ (K)	4552 ± 154	`ARES` + `MOOG`
$v \sin i_*$ (km s^{-1})	1.86 ± 0.50	`ARES` + `MOOG`
Age (Gyr)	$5.4^{+6.3}_{-5.0}$	Isochrones
Stellar abundances		
[Fe/H] (dex)	-0.284 ± -0.067	`ARES` + `MOOG`
[Mg/H] (dex)	-0.23 ± 0.17	`ARES` + `MOOG`
[Si/H] (dex)	-0.29 ± 0.20	`ARES` + `MOOG`
Galactic space velocity components		
U (km s^{-1})	-35.6 ± 0.7	*Gaia* EDR3
V (km s^{-1})	-10.7 ± 0.3	*Gaia* EDR3
W (km s^{-1})	-3.50 ± 0.5	*Gaia* EDR3

Note. Sources: `exoplanet` (Foreman-Mackey et al. 2021a; Foreman-Mackey et al. 2021c), `ARES` (Sousa et al. 2015), `MOOG` (Sneden 1973; Kurucz 1993), *Gaia* (Gaia Collaboration 2021)

note that we do not subtract the Solar motion and compute the U, V, and W values in the right-handed system.

We also use the approach of Reddy, Lambert & Allende Prieto (2006) in a Monte Carlo fashion with 100 000 samples to determine the probability that TOI-836 is in a given kinematic Galactic family, using a weighted average of the results obtained using the velocity dispersion standards of Bensby, Feltzing & Lundström (2003), Bensby, Feltzing & Oey (2014), Reddy et al. (2006), and Chen et al. (2021). We find a Galactic thin disc membership probability for TOI-836 of 98.9 per cent, thick disc membership probability of 1.1 per cent, and halo membership probability of 0 per cent. This agrees well with the Galactic eccentricity of TOI-836 of 0.08, and the high Galactic Z-component of the angular momentum of $Z \approx 1770$ kpc km s^{-1}. We compute these values using the `galpy` package after a Galactic orbit determination using the *Gaia* EDR3 position, proper motions, and parallax, and *Gaia* DR2 radial velocity integrating over 5 Gyr, as well as the typical values for [Mg/H] and [Si/H] from stellar analysis.

3.2 Exoplanet data analysis

We model the photometric and spectroscopic data presented in Section 2 using the `exoplanet` package (Foreman-Mackey et al. 2021a; Foreman-Mackey et al. 2021c), which incorporates `starry` (Luger et al. 2019), `celerite` (Foreman-Mackey et al. 2017), and `PyMC3` (Salvatier, Wiecki & Fonnesbeck 2016) within its framework. We have selected the high-quality follow-up light curves, which includes all observations from *TESS* and *CHEOPS* as our space-based photometry, one observation from *NGTS*, nine observations from *LCOGT*, one observation from *ASTEP*, and one observation from *MEarth* as our ground-based photometry sample (see Table 2). Our radial velocity modelling of short-term trends is comprised of data from *HARPS* and *PFS*.

Table 7. Timing offsets for observations of TOI-836 b and TOI-836 c.

Facility	UT night	δT_c (d)	δT_c error (d)
TOI-836 b			
TESS S11	–	0.009757	0.005609
TESS S11	–	0.002165	0.002800
TESS S11	–	0.003431	0.005132
TESS S11	–	0.000558	0.003520
TESS S11	–	0.002330	0.004450
TESS S11	–	0.001242	0.003252
LCOGT-CTIO	2020 Mar 8	–	–
LCOGT-SSO	2020 Mar 20	–	–
LCOGT-SSO	2020 May 4	–	–
CHEOPS	2020 Jul 8	0.0061575	0.002024
TESS S38	–	–	–
TESS S38	–	−0.000887	0.007903
TESS S38	–	0.006464	0.006724
TESS S38	–	–	–
TESS S38	–	0.0021850	0.004691
TESS S38	–	−0.001041	0.006310
TESS S38	–	–	–
TOI-836 c			
TESS S11	–	0.0034651	0.000826
TESS S11	–	0.0033399	0.001295
MEarth-South	2019 Jul 4	0.0035104	0.000811
LCOGT-SSO	2020 Feb 29	–	–
LCOGT-SSO	2020 Apr 12	0.0182677	0.001780
LCOGT-SAAO	2020 May 16	−0.0148950	0.005903
CHEOPS	2020 May 25	−0.0166364	0.000806
CHEOPS	2020 Jun 28	−0.0181972	0.001690
CHEOPS	2020 Jul 7	−0.0234211	0.000923
LCOGT-SSO	2021 Apr 8	0.0027583	0.003884
ASTEP	2021 Apr 8	–	–
NGTS	2021 Apr 16	−0.0011893	0.001562
LCOGT-CTIO	2021 Apr 16	0.0007001	0.001320
LCOGT-CTIO	2021 Jun 24	−0.0010068	0.001712
CHEOPS	2021 May 4	0.0007432	0.000622
TESS S38	–	−0.0006412	0.001347
TESS S38	–	−0.0002651	0.001231
TESS S38	–	0.0097779	0.001272

Note. Sources: *LCOGT* (Brown et al. 2013), *CHEOPS* (Benz et al. 2021), *ASTEP* (Daban et al. 2010), *NGTS* (Wheatley et al. 2018), *MEarth-South* (Irwin et al. 2015b), *TESS* (Ricker et al. 2015).

3.2.1 *Transit timing variations*

In order to account for perceived TTVs on TOI-836 c in 2020 (year 2 of observation), we introduce an offset parameter T_c. This offset parameter is calculated by fitting each detrended, normalized data set using the `EXOFAST` modelling tool (Eastman, Gaudi & Agol 2013; Eastman et al. 2019). The offset parameter represents the value of the central transit time found in `EXOFAST`, and δT_c is the difference from the expected transit ephemeris. The corresponding δT_c for each transit can be found in Table 7. We omit offset parameters for the transits of TOI-836 b taken by *LCOGT*, as these observations are not of sufficient precision to allow for suitably accurate determination of the offset parameter. We omit offset parameters for the *LCOGT* transit of TOI-836 c on 2020 February 29 and the *ASTEP* transit on 2021 April 8 for these same reasons. We also choose to omit transits of both planets in the *TESS* light curves that occur very close to the start and end of sectors and close to the data download gap, as they are likely to be highly affected by systematics which may affect transit timings.

We plot the resulting offset for the central transit time T_c for each of TOI-836 b and TOI-836 c in Fig. 9. We note that there appear to be

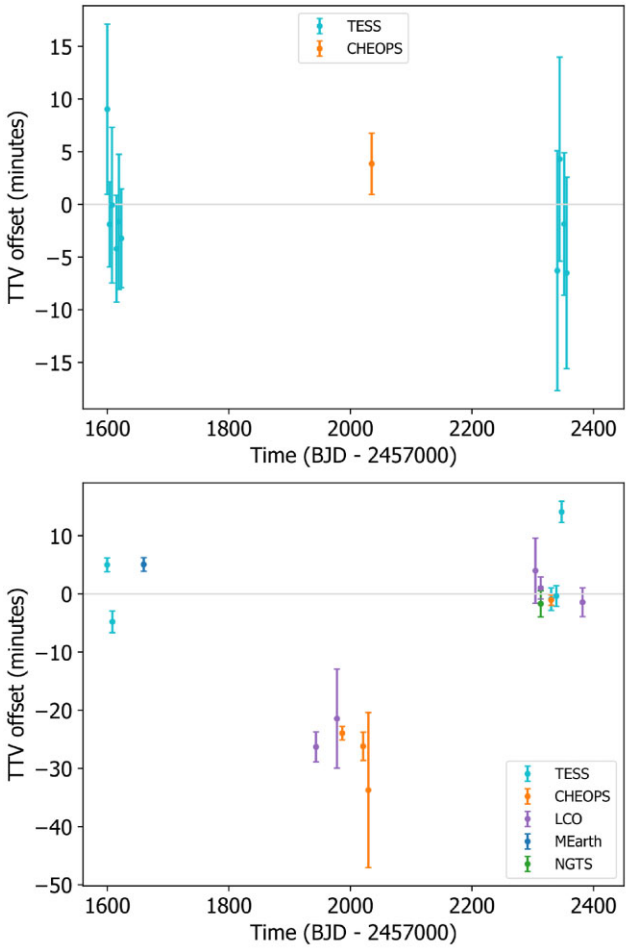

Figure 9. Top panel: Transit timing variations (TTVs) for each transit of TOI-836 b from the following photometry sources: *TESS* in turquoise and *CHEOPS* in yellow. Bottom panel: TTVs for each transit of TOI-836 c from the following photometry sources: *TESS* in turquoise, *CHEOPS* in yellow, *LCOGT* in purple, *MEarth-South* in blue, and *NGTS* in green.

no significant TTVs in the observed transits of TOI-836 b, however in TOI-836 c we detect an offset within the T_c values ranging from approximately 20 to 30 min. The presence of these TTVs is supported by observations from both the space-based *CHEOPS* satellite and multiple ground-based facilities. These TTV measurements alone are not enough to be able to put meaningful constraints on the mass of TOI-836 c, but with further TTV monitoring it may be possible.

3.2.2 *Radial velocity (RV)*

We model the radial velocity of TOI-836 using the *HARPS* and *PFS* data simultaneously, seen in Fig. 10. We analysed these radial velocity data with various models, including linear and quadratic drift and a third planet. None of these were able to account for the large scatter in the radial velocity measurements, and therefore we find it necessary to apply a GP model for both of our chosen data sets in order to account for stellar variability. We apply a quasi-periodic kernel (commonly used in works with similar goals, such as Osborn et al. 2021), as implemented in `celerite`. We assign a prior probability distribution for the rotation period as a normal distribution centred around 22 d, with a standard deviation of 0.1 d, based on the results from the *WASP-South* periodogram. In completion, our kernel is a combination of two available kernels in the `PyMC3` package[6] (Salvatier et al. 2016) – the `Periodic` and `ExpQuad` kernels are multiplied to create the final quasi-periodic kernel. As part of this analysis, we define a set of GP hyperparameters which are fit concurrently for both sets of radial velocity data: η representing the GP amplitude, the stellar rotation period P, the smoothing parameter l_P, and the time-scale of active region evolution l_E. This has been shown to successfully model stellar activity in e.g. Grunblatt, Howard & Haywood (2015), Santerne et al. (2018), and Osborn et al. (2021).

When modelling the HARPS and PFS data, we utilize `exoplanet` to find values for the radial velocity semi-amplitude K with priors from 0 to 10 $\mathrm{m\,s^{-1}}$. We also fit for values for the offsets as a normal distribution centred around the mean of the radial velocity of each data set. We also fit for jitter terms centred around the minimum radial velocity error multiplied by 2, which represent other variability not accounted for in the HARPS and PFS formal uncertainties, and the application of the GP model to the data.

Modelled planetary reflex motions are subtracted from the radial velocities at each timestamp before being passed to the GP kernel, and we use the same time system for both the HARPS and PFS data sets (BJD - 2457000). The prior distributions for each of the parameters used in the code can be found in Appendix Tables A1, A2, and A3 for the host star TOI-836, and the planets TOI-836 b and TOI-836 c, respectively.

3.2.3 *Joint fitting*

To bring the two observational methods together, we utilize the `exoplanet` package to fit for our initial values from the maximum log probability, which are then passed into the `PyMC3` sampler as a starting point in a No U-Turn Sampler (NUTS) variant of the Hamilton Monte Carlo (HMC) algorithm (Hoffman & Gelman 2011). We set our run to have a burn-in of 4000 samples, 4000 steps, and 10 chains, giving our modelling significant opportunity to explore the parameter spaces.

As a result of our joint fitting of transit and radial velocity data, we find that TOI-836 b is a super-Earth planet with a radius of $1.70 \pm 0.07\,\mathrm{R_\oplus}$ and mass of $4.5 \pm 0.9\,\mathrm{M_\oplus}$, on a period of 3.82 d, and TOI-836 c is a sub-Neptune planet with a radius of $2.59 \pm 0.09\,\mathrm{R_\oplus}$ and mass of $9.6 \pm 2.6\,\mathrm{M_\oplus}$ on a period of 8.60 d. From this we can infer a bulk density of $5.02^{+0.36}_{-0.44}\,\mathrm{g\,cm^{-3}}$ for TOI-836 b, and $3.06^{+0.47}_{-0.54}\,\mathrm{g\,cm^{-3}}$ for TOI-836 c. A full set of parameters for TOI-836 can be found in Table 6, and parameters for each planet can be found in Table 8.

3.2.4 *Long-term trends*

In addition to our short-term radial velocity analysis with data from HARPS and PFS, we also make use of HIRES data to constrain longer term trends. We fit the data for a linear drift, and find a drift value of $-7.95 \pm 2.14\,\mathrm{m\,s^{-1}\,yr^{-1}}$. The fit is shown in Fig. 11. The HIRES data are sparsely sampled over a duration of approximately 4 yr. Therefore it is not possible to remove the stellar activity signal in the manner we did for the HARPS and PFS data, and so the marginally detected linear trend may not be real, and we do not use this trend when fitting the radial velocities in Section 3.2.2. However the HIRES data are able to rule out any radial velocity drift above

[6] https://docs.pymc.io/api/gp/cov.html

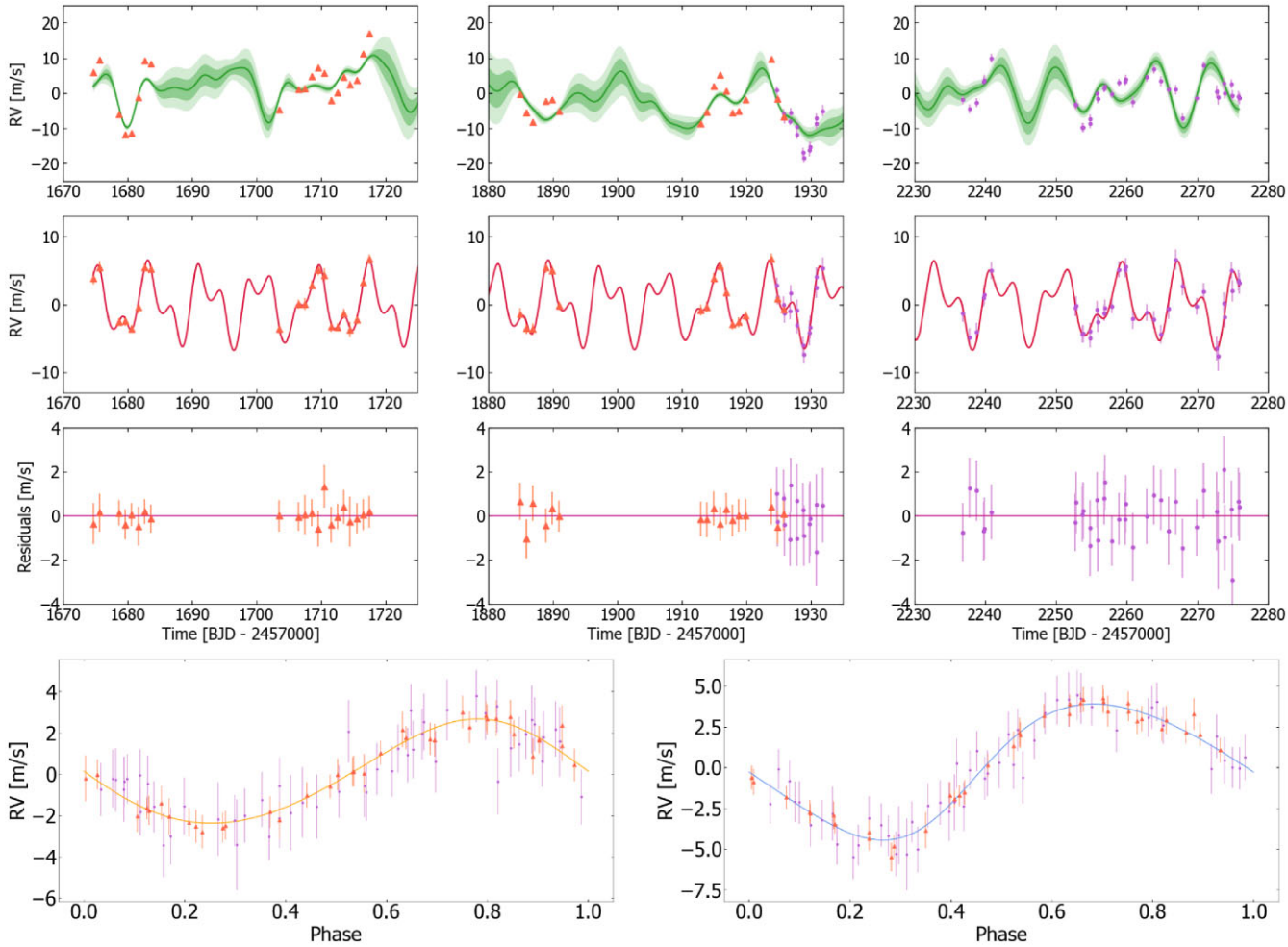

Figure 10. Top panels: HARPS (purple circles) and PFS (orange triangles) RV data with formal uncertainties with the GP model plotted as a solid green line, with 1 and 2 standard deviations in lighter shades. Second panels: Combined RV models of the two planets, with the GP subtracted, with HARPS and PFS RV datapoints. Third panels: Residuals for HARPS and PFS datapoints relative to a baseline RV of 0 $m\,s^{-1}$. Fourth panels (left-hand panel): HARPS (purple circles) and PFS (orange triangles) RV data, phase-folded to a period corresponding to that of TOI-836 b with the RV model shown in orange. Fourth panels (right-hand panel): HARPS and PFS data, phase-folded to a period corresponding to that of TOI-836 c with the RV model shown in blue.

the level of the stellar activity signal ($\sim 10\,m\,s^{-1}$) over a 4 yr time period.

4 DISCUSSION

In addition to the results from our joint modelling, we find that TOI-836 has a relatively low metallicity of [Fe/H] $= -0.284 \pm -0.067$ dex. As was found in Adibekyan et al. (2021), there is a strong trend between host stellar metallicity and the iron component for low-mass exoplanets. This can be interpreted as systems that formed from metal-rich proto-stellar/planetary discs have stars with metal-rich photospheres and planets with large metallic cores. This is supported by the recent study of Wilson et al. (2022) that found a correlation between sub-Neptune planet densities and stellar metallicities across all stellar types that implies that sub-Neptunes around metal-rich stars have larger metallic cores that can retain a larger atmosphere and hence appear less dense. This effect has also been observed in radius valley trends with metallicity (Chen et al. 2022). As TOI-836 has a low-metallicity we reproduce fig. 15 of Wilson et al. (2022) and plot the bulk densities of the two planets against the stellar metallicity in Fig. 12, alongside a sample of planets orbiting K-dwarfs with a radius of $<4\,R_\oplus$ and a density of $<15\,g\,cm^{-3}$ from the NASA Exoplanet Archive. This sample of all well-characterized super-Earths and sub-Neptunes around K-dwarfs supports previous findings and strengthens the evidence that stellar composition affects planetary internal structure.

4.1 Positions of the planets on the mass–radius (M-R) diagram

We plot TOI-836 b and TOI-836 c on the mass–radius (M-R) diagram in Fig. 13, using `fancy-massradius-plot`,[7] alongside a sample of exoplanets from the *TEPCAT* catalogue (Southworth 2011). It can be seen that TOI-836 b sits directly between the $MgSiO_3$ and 50 per cent Fe–50 per cent $MgSiO_3$ planetary composition models from Zeng et al. (2016), and TOI-836 c sits on the H_2O track. The masses and radii of TOI-836 b and TOI-836 c, along with their bulk densities, are consistent with the previously determined populations of super-Earths and mini-Neptunes.

[7] https://github.com/oscaribv/fancy-massradius-plot

Table 8. Parameters of TOI-836 b and TOI-836 c.

Property	Value	
	TOI-836 b	**TOI-836 c**
Identifier	TOI-836.02	TOI-836.01
Period (d)	3.81673 ± 0.00001	8.59545 ± 0.00001
Mass ($M_\oplus$)	$4.53^{+0.92}_{-0.86}$	$9.6^{+2.7}_{-2.5}$
Radius ($R_\oplus$)	1.704 ± 0.067	2.587 ± 0.088
Density (gccc)	$5.02^{+0.36}_{-0.44}$	$3.06^{+0.48}_{-0.54}$
R_p/R_*	0.0235 ± 0.0013	0.0357 ± 0.0018
T_c (TBJD)	1599.9953 ± 0.0019	1599.7623 ± 0.0008
T1-T4 duration (h)	$1.805^{+0.222}_{-0.007}$	$2.486^{+0.161}_{-0.192}$
T2-T3 duration (h)	$1.6823^{+0.0012}_{-0.3292}$	$2.256^{+0.144}_{-0.432}$
Impact parameter	0.58 ± 0.11	0.53 ± 0.13
K ($m\,s^{-1}$)	2.38 ± 0.35	3.86 ± 0.85
Inclination (°)	87.57 ± 0.44	88.7 ± 1.5
Semimajor axis (AU)	0.04220 ± 0.00093	0.0750 ± 0.0016
Temperature T_{eq} (K) *	871 ± 36	665 ± 27
Insolation flux ($S_\odot$)	78.838 ± 0.015	26.707 ± 0.003
Eccentricity	0.053 ± 0.042	0.078 ± 0.056
Argument of periastron (°)	9 ± 92	-28 ± 113
TSM	65.7 ± 5.8	82.4 ± 5.8

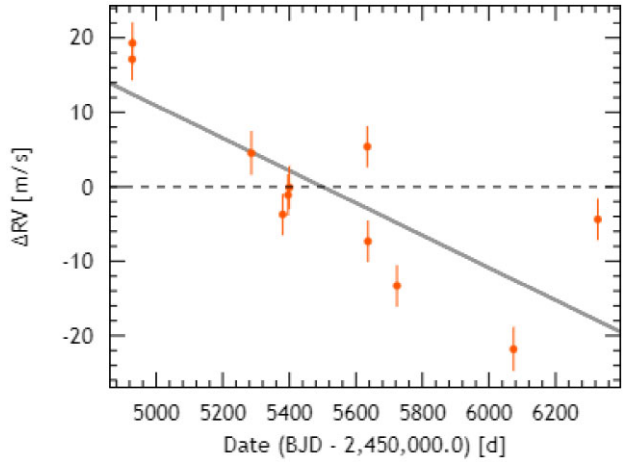

Figure 11. Radial velocity data of TOI-836 from the HIRES instrument on the *Keck* telescope from 2009 April 6 to 2013 February 3, and fit with a linear trend represented by the solid grey line.

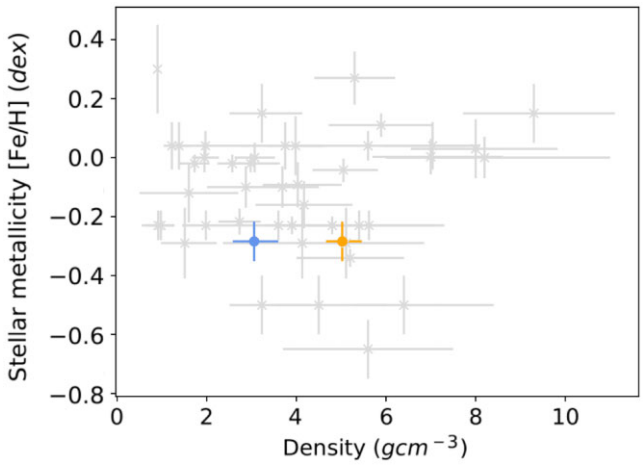

Figure 12. Bulk densities of TOI-836 b (orange) and TOI-836 c (blue) plotted against the stellar metallicity of TOI-836, along with a sample of planets orbiting K-dwarfs with $R < 4\,R_\oplus$ and $\rho < 15\,g\,cm^{-3}$.

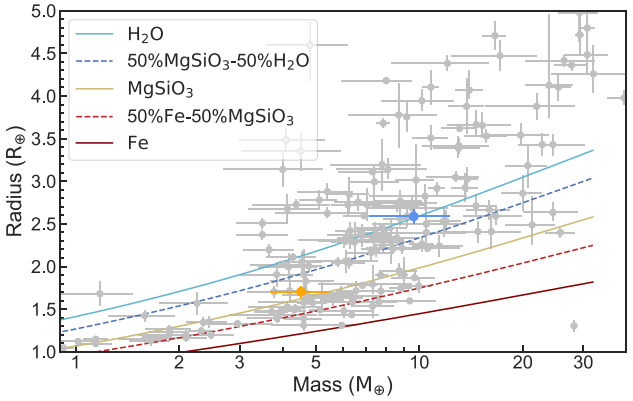

Figure 13. Mass–radius diagram plotted for TOI-836 b in orange and TOI-836 c with exoplanets from the *TEPCAT* catalogue (Southworth 2011) in grey and composition models from Zeng, Sasselov & Jacobsen (2016).

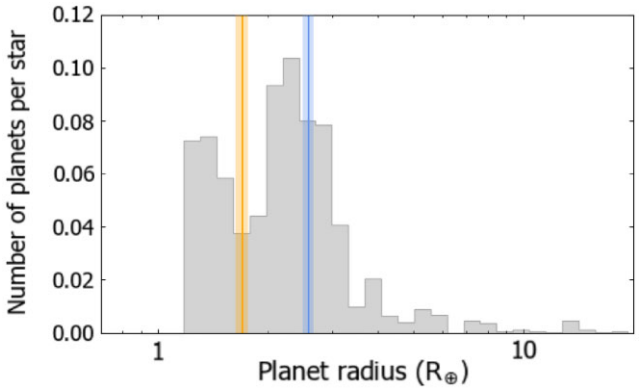

Figure 14. Histogram of confirmed planets with periods less than 100 d, using data from Fulton & Petigura (2018) represented in grey, overplotted with the radii of TOI-836 b in orange and TOI-836 c in blue, including 1σ standard deviations according to Table 8.

4.2 Internal structure modelling

Using the planetary and stellar parameters derived above, we used a Bayesian analysis to infer the internal structure of both planets. The method we use is presented in detail in Leleu et al. (2021); we just recall here the main elements. The Bayesian analysis relies on two parts. The first one is the forward models which allows computing the planetary radius as a function of internal structure parameters, here the mass of the solid Fe/Si core, the fraction of Fe in the core, the mass of the silicate mantle, and its composition (Si, Mg, and Fe molar ratios), the mass of the water layer, the mass of the gas envelope (composed in this model of pure H/He), the equilibrium temperature of the planet, and its age. The second part is the Bayesian inference itself.

The details of the forward model are given in Leleu et al. (2021), we just emphasize the fact that the gaseous (H/He) part of the planet does not influence, in our model, the 'non-gas' part of the planet (core, mantle, and water layer). The radius of the non-gas part is not influenced by the potential compression and thermal isolation effect from the gas envelope. The molar ratio of Fe, Si, and Mg in the refractory parts of the two planets (core and mantle) are assumed to be identical and similar to the one of the star. Note, however, that Adibekyan et al. (2021) recently showed that the stellar and planetary abundances may not be always correlated in a one-to-one relation.

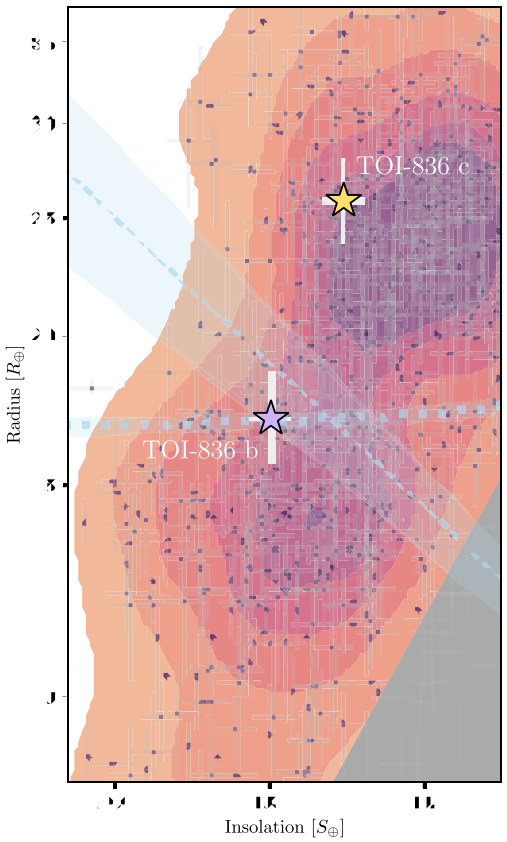

Figure 15. TOI-836 b and TOI-836 c (filled stars) as a function of planetary radius and insolation, compared with the population of exoplanets. Colours represent a kernel density estimation (KDE) applied to small ($R_p < 4\,R_\oplus$), transiting planets retrieved from the NASA Exoplanet Archive (Akeson et al. 2013b). The dashed line (and associated 1-σ error band) shows the estimate for the position of the evaporation valley from Martinez et al. (2019), while the dotted line shows a boundary due to gas-depleted formation derived from cool stars in *Kepler* and K2, converted to insolation using stellar parameters for TOI-836 (Cloutier & Menou 2020).

The water and gas mass ratio, on the other hand, are not required to be similar between the two planets. In terms of priors, we assume that the core, mantle, and water mass fraction (relative to the non-gas part) are uniform (subject to the constraint that they add up to one), whereas the mass fraction of the H/He layer is assumed to be uniform in log. We point out the fact that considering, instead, a uniform prior for the H/He gas layer would translate to more gas-rich planets, and consequently less water-rich planets.

The resulting internal structure of both planets presented are summarized in Table 9. TOI-836 b is likely to contain a very small fraction of gas, and could have a non-negligible mass of water (although the solution with no water is also compatible with the data). TOI-836 c, on the other hand, has a much smaller density and is likely to contain more gas and/or water. We finally recall that the derived internal structure results from a Bayesian analysis, and that the distributions are of statistical nature and depend somewhat on the assumed priors.

The structure of TOI-836 b is somewhat analogous to that of TOI-1235 b (Cloutier et al. 2020), despite the difference in the host star's spectral type, and the rocky composition of the planet may support a thermally driven or core-powered mass-loss scenario rather than a gas-poor formation scenario. TOI-836 c, on the other hand, is a little more ambiguous, but given its insolation flux of $26.707 \pm 0.003\,S_\odot$ and radius of $2.59 \pm 0.09\,R_\oplus$, we expect a non-negligible fraction of its mass to be in gaseous form.

Table 9. Interior structure properties of TOI-836 b and TOI-836 c.

Property (unit)	Values	
	TOI-836 b	TOI-836 c
M_{core}/M_{total}	$0.12^{+0.16}_{-0.11}$	$0.10^{+0.15}_{-0.09}$
M_{water}/M_{total}	$0.18^{+0.25}_{-0.16}$	$0.33^{+0.15}_{-0.28}$
$\log(M_{gas})$	$-8.33^{+3.95}_{-3.30}$	$-1.99^{+0.93}_{-6.77}$
Fe_{core}	$0.90^{+0.09}_{-0.08}$	$0.90^{+0.09}_{-0.08}$
Si_{mantle}	$0.41^{+0.08}_{-0.07}$	$0.41^{+0.08}_{-0.07}$
Mg_{mantle}	$0.45^{+0.15}_{-0.17}$	$0.44^{+0.15}_{-0.17}$

These two planets may also support the concept of intrasystem uniformity reported by Millholland, Wang & Laughlin (2017) and Millholland & Winn (2021), as the two planets lie close together within the mass–radius space than if two planets were to be drawn at random from the entire distribution of exoplanets according to their radii.

4.3 Positions of the planets compared to the radius valley

The radius valley is a bimodal distribution of planetary radii that separates super-Earths and sub-Neptunes either side of $R_p \approx 2\,R_\oplus$ (Fulton et al. 2017; Van Eylen et al. 2018), from $\approx 1.3\,R_\oplus$ and $\approx 2.6\,R_\oplus$, respectively. The radius valley is important to examine on the basis of its implications for the formation and evolution of terrestrial planets (Giacalone et al. 2022). Some commonalities can be found within the population of super-Earths on the left-hand side of the valley, consisting of atmosphere-stripped rocky cores, and the population of mini-Neptunes on the right-hand side, consisting of rocky cores that have retained their atmospheres (Van Eylen et al. 2021). Many possibilities for the origin of the radius valley have been speculated, including the theory that terrestrial planets lose their atmospheres through photoevaporation (Owen & Wu 2013; Jin & Mordasini 2018; Van Eylen et al. 2021), mass-loss due to core temperatures (Ginzburg, Schlichting & Sari 2016), and the impacts of planetesimals (Schlichting, Sari & Yalinewich 2015).

In Fig. 14 we plot a histogram of planets with orbital periods less than 100 d based on data from Fulton & Petigura (2018), along with the positions of TOI-836 b and TOI-836 c using the modelled values from `exoplanet` in Table 8. We also plot a diagram of planetary radius against the insolation fluxes in Fig. 15, alongside a sample of the exoplanet population and the position of the radius valley as estimated by Martinez et al. (2019). TOI-836 b can be seen to sit directly within this valley, and TOI-836 c can be seen close to the peak on the higher radius side of the valley. TOI-836 b is set at a particularly interesting location, and there may be scope for further investigation of the extent and composition of its atmosphere, especially as the host star is suspected to not be young in age (see Section 3.1).

In order to evaluate TOI-836 as a potential target for transmission spectroscopy follow-up in the era of *JWST* (Gardner et al. 2006), we calculate a Transmission Spectroscopy Metric (TSM) for each of the planets based upon equation 1 in Kempton et al. (2018). This value is an estimate of the observed SNR of each planet as would be achieved by the *NIRSPEC* instrument on *JWST*. We find a TSM for TOI-836 b of 65.7, and a TSM for TOI-836 c of 82.4 (see Table 8). We also note that the system has been allocated time on *JWST* as can be

seen in Batalha et al. (2021), with the intention of further examining the atmospheric characteristics of TOI-836 b and TOI-836 c through molecular abundances. The precise masses provided in this paper will greatly help in the characterization of the atmospheres of these planets.

5 CONCLUSION

In this paper, we have presented the TOI-836 system and the discovery of its two planets, TOI-836 b and TOI-836 c. We base our discovery upon data from two sectors of *TESS* data (11 and 38 from year 1 and year 3, respectively) at 2-min cadence, and a further five space-based observations ranging from 2020 to 2021 from *CHEOPS*, which are complemented by ground-based photometry from the *NGTS*, *MEarth*, *LCOGT*, and *ASTEP* facilities, with supporting evidence for a stellar rotation period of 21.99 ± 0.097 d supported by data from *WASP-South*. We model this photometry data jointly with radial velocity data from HARPS and PFS using the `exoplanet` package to constrain short-term trends, and HIRES data for long-term trends. We are also able to rule out the presence of blended stellar companions that may affect our photometry from an examination of the imaging from *Gemini*-Zorro. The planets orbit a K-type dwarf star with a mass of $0.68 \pm 0.05\,M_{\odot}$ and a radius of $0.67 \pm 0.01\,R_{\odot}$.

TOI-836 b is a super-Earth planet with a mass of $4.5 \pm 0.9\,M_{\oplus}$ and a radius of $1.70 \pm 0.07\,R_{\oplus}$, on an orbit of 3.82 d. Our internal structure modelling indicates that this planet possesses a relatively small fraction of its mass in the form of gas.

TOI-836 c is a sub-Neptune with a mass of $9.6 \pm 2.6\,M_{\oplus}$ and a radius of $2.59 \pm 0.09\,R_{\oplus}$, on an orbit of 8.60 d. Our structure modelling indicates that it contains a higher proportion of gas and/or water than TOI-836 b. We also find significant TTVs within our observations of this planet, which may indicate the presence of a third non-transiting planet in the system – however we find no transits of a third planet within our current set of photometry data, or any indication of an additional periodic signal in our current radial velocity data.

TOI-836 b appears in the centre of the radius valley, and TOI-836 c appears to sit close to the peak on the right-hand side of the valley, which is an area of interest in terms of the formation and structure of terrestrial planets and the dynamics of atmospheric loss and retention. The planets also contribute to the *TESS* Level 1 Mission requirement, and are particularly amenable to follow-up observations in the era of *JWST*.

ACKNOWLEDGEMENTS

This work makes use of `tpfplotter` by J. Lillo-Box (publicly available in www.github.com/jlillo/tpfplotter), which also made use of the python packages `astropy`, `lightkurve`, `matplotlib`, and `numpy`.

This research makes use of `exoplanet` (Foreman-Mackey et al. 2021b) and its dependencies (Astropy Collaboration 2013, 2018; Kipping 2013b; Salvatier et al. 2016a; Theano Development Team 2016; Kumar et al. 2019; Luger et al. 2019; Agol, Luger & Foreman-Mackey 2020; Foreman-Mackey et al. 2021b).

This paper makes use of `EXOFAST` (Eastman et al. 2013, 2019) as provided by the NASA Exoplanet Archive, which is operated by the California Institute of Technology, under contract with the National Aeronautics and Space Administration under the Exoplanet Exploration Program.

This publication makes use of The Data & Analysis Center for Exoplanets (DACE), which is a facility based at the University of Geneva (CH) dedicated to extrasolar planets data visualisation, exchange, and analysis. DACE is a platform of the Swiss National Centre of Competence in Research (NCCR) PlanetS, federating the Swiss expertise in Exoplanet research. The DACE platform is available at https://dace.unige.ch.

This work makes use of data from the European Space Agency (ESA) mission *Gaia* (https://www.cosmos.esa.int/gaia), processed by the *Gaia* Data Processing and Analysis Consortium (DPAC, https://www.cosmos.esa.int/web/gaia/dpac/consortium). Funding for the DPAC has been provided by national institutions, in particular the institutions participating in the *Gaia* Multilateral Agreement.

This paper includes data collected by the *TESS* mission. Funding for the *TESS* mission is provided by the NASA Explorer Program. Resources supporting this work were provided by the NASA High-End Computing (HEC) Program through the NASA Advanced Supercomputing (NAS) Division at Ames Research Center for the production of the SPOC data products. The TESS team shall assure that the masses of fifty (50) planets with radii less than 4 REarth are determined.

We acknowledge the use of public *TESS* Alert data from pipelines at the *TESS* Science Office and at the *TESS* Science Processing Operations Center.

This research makes use of the Exoplanet Follow-up Observation Program website, which is operated by the California Institute of Technology, under contract with the National Aeronautics and Space Administration under the Exoplanet Exploration Program.

This paper includes data collected by the TESS mission that are publicly available from the Mikulski Archive for Space Telescopes (MAST).

CHEOPS is an ESA mission in partnership with Switzerland with important contributions to the payload and the ground segment from Austria, Belgium, France, Germany, Hungary, Italy, Portugal, Spain, Sweden, and the United Kingdom. The CHEOPS Consortium would like to gratefully acknowledge the support received by all the agencies, offices, universities, and industries involved. Their flexibility and willingness to explore new approaches were essential to the success of this mission.

This paper is in part based on data collected under the NGTS project at the ESO La Silla Paranal Observatory. The NGTS facility is operated by the consortium institutes with support from the UK Science and Technology Facilities Council (STFC) projects ST/M001962/1 and ST/S002642/1.

The MEarth Team gratefully acknowledges funding from the David and Lucile Packard Fellowship for Science and Engineering (awarded to D.C.). This material is based upon work supported by the National Science Foundation under grants AST-0807690, AST-1109468, AST-1004488 (Alan T. Waterman Award), and AST-1616624, and upon work supported by the National Aeronautics and Space Administration under Grant No. 80NSSC18K0476 issued through the XRP Program. This work is made possible by a grant from the John Templeton Foundation. The opinions expressed in this publication are those of the authors and do not necessarily reflect the views of the John Templeton Foundation.

This work makes use of observations from the LCOGT network. Part of the LCOGT telescope time was granted by NOIRLab through the Mid-Scale Innovations Program (MSIP). MSIP is funded by NSF.

The *ASTEP* project was funded by the Agence Nationale de la Recherche (ANR), the Institut National des Sciences de l'Univers (INSU), the Programme National de Planétologie (PNP), and the Idex UCAJEDI (ANR-15-IDEX-01). The logistics at Concordia is handled by the French Institut Paul-Emile Victor (IPEV) and the Italian Programma Nazionale di Ricerche in Antartide (PNRA).

We acknowledge support from the European Space Agency SCI-S Faculty Research Project Programme. This research is supported by the European Research Council (ERC) under the European Union's Horizon 2020 research and innovation programme (grant agreement n° 803193/BEBOP), and from the Science and Technology Facilities Council (STFC; grant n° ST/S00193X/1).

WASP-South is hosted by the South African Astronomical Observatory and we are grateful for their ongoing support and assistance. Funding for WASP comes from consortium universities and from the UK's Science and Technology Facilities Council.

This study is based on observations collected at the European Southern Observatory under ESO programme 1102.C-0249 (PI: Armstrong).

This paper includes data gathered with the 6.5-m Magellan Telescopes located at Las Campanas Observatory, Chile.

MINERVA-Australis is supported by Australian Research Council LIEF Grant LE160100001, Discovery Grants DP180100972 and DP220100365, Mount Cuba Astronomical Foundation, and institutional partners University of Southern Queensland, UNSW Sydney, MIT, Nanjing University, George Mason University, University of Louisville, University of California Riverside, University of Florida, and The University of Texas at Austin.

We respectfully acknowledge the traditional custodians of all lands throughout Australia, and recognize their continued cultural and spiritual connection to the land, waterways, cosmos, and community. We pay our deepest respects to all Elders, ancestors, and descendants of the Giabal, Jarowair, and Kambuwal nations, upon whose lands the *MINERVA-Australis* facility at Mt Kent is situated.

Supported by the international Gemini Observatory, a program of NSF's NOIRLab, which is managed by the Association of Universities for Research in Astronomy (AURA) under a cooperative agreement with the National Science Foundation, on behalf of the Gemini partnership of Argentina, Brazil, Canada, Chile, the Republic of Korea, and the United States of America.

Some of the observations in the paper make use of the High-Resolution Imaging instrument(s) 'Alopeke and Zorro. 'Alopeke and Zorro were funded by the NASA Exoplanet Exploration Program and built at the NASA Ames Research Center by Steve B. Howell, Nic Scott, Elliott P. Horch, and Emmett Quigley. 'Alopeke and Zorro were mounted on the Gemini North and South telescopes of the international Gemini Observatory, a program of NSF's NOIRLab, which is managed by the Association of Universities for Research in Astronomy (AURA) under a cooperative agreement with the National Science Foundation. on behalf of the Gemini partnership: the National Science Foundation (United States), National Research Council (Canada), Agencia Nacional de Investigación y Desarrollo (Chile), Ministerio de Ciencia, Tecnología e Innovación (Argentina), Ministério da Ciência, Tecnologia, Inovações e Comunicações (Brazil), and Korea Astronomy and Space Science Institute (Republic of Korea).

This work has been carried out within the framework of the NCCR PlanetS supported by the Swiss National Science Foundation.

FH is supported by an STFC studentship. The French group acknowledges financial support from the French Programme National de Planétologie (PNP, INSU). AO is supported by an STFC studentship. This work has been carried out within the framework of the NCCR PlanetS supported by the Swiss National Science Foundation. MNG acknowledges support from the European Space Agency (ESA) as an ESA Research Fellow. DJA acknowledges support from the STFC via an Ernest Rutherford Fellowship (ST/R00384X/1). PJW acknowledges support from STFC consolidated grant ST/T000406/1. JSJ greatfully acknowledges support by FONDECYT grant 1201371 and from the ANID BASAL projects ACE210002 and FB210003. JL-B acknowledges financial support received from 'la Caixa' Foundation (ID 100010434) with fellowship code LCF/BQ/PI20/11760023, and the Projects No. PID2019-107061GB-C61 and No. MDM-2017-0737. EDM acknowledges the support from Fundação para a Ciência e a Tecnologia (FCT) by the Investigador FCT contract IF/00849/2015/CP1273/CT0003. SH acknowledges CNES funding through the grant 837319. We acknowledge the support by FCT - Fundação para a Ciência e a Tecnologia through national funds and by FEDER through COMPETE2020 - Programa Operacional Competitividade e Internacionalização by these grants: UID/FIS/04434/2019; UIDB/04434/2020; UIDP/04434/2020; PTDC/FIS-AST/32113/2017 & POCI-01-0145-FEDER-032113; PTDC/FISAST/28953/2017 & POCI-01-0145-FEDER-028953. SGS acknowledges the support from FCT through Investigador FCT contract nr. CEECIND/00826/2018 and POPH/FSE (EC). SMO is supported by an STFC studentship. VA acknowledges the support from FCT by the Investigador FCT contract IF/00650/2015/CP1273/CT0001. TGW, ACC, and KH acknowledge support from STFC consolidated grant numbers ST/R000824/1 and ST/V000861/1, and UKSA grant ST/R003203/1. YA and MJH acknowledge the support of the Swiss National Fund under grant 200020_172746. SCCB acknowledges support from FCT through FCT contracts nr. IF/01312/2014/CP1215/CT0004. XB and SC acknowledge their role as ESA-appointed CHEOPS science team members. ABr was supported by the SNSA. This project was supported by the CNES. The Belgian participation to CHEOPS has been supported by the Belgian Federal Science Policy Office (BELSPO) in the framework of the PRODEX Program, and by the University of Liège through an ARC grant for Concerted Research Actions financed by the Wallonia-Brussels Federation; LD is an F.R.S.-FNRS Postdoctoral Researcher. ODSD is supported in the form of work contract (DL 57/2016/CP1364/CT0004) funded by national funds through FCT. B-OD acknowledges support from the Swiss National Science Foundation (PP00P2-190080). This project has received funding from the European Research Council (ERC) under the European Union's Horizon 2020 research and innovation programme (project FOUR ACES; grant agreement No 724427). It has also been carried out in the frame of the National Centre for Competence in Research PlanetS supported by the Swiss National Science Foundation (SNSF). DE acknowledges financial support from the Swiss National Science Foundation for project 200021_200726. MF and CMP gratefully acknowledge the support of the Swedish National Space Agency (DNR 65/19, 174/18). MF acknowledges their role as ESA-appointed CHEOPS science team members. DG gratefully acknowledges financial support from the CRT foundation under Grant No. 2018.2323 'Gaseousor rocky? Unveiling the nature of small worlds'. DG acknowledges their role as ESA-appointed CHEOPS science team members. MG is an F.R.S.-FNRS Senior Research Associate. This work was granted access to the HPC resources of MesoPSL financed by the Region Ile de France and the project Equip@Meso (reference ANR-10-EQPX-29-01) of the programme Investissements d'Avenir supervised by the Agence Nationale pour la Recherche. JL acknowledges their role as ESA-appointed CHEOPS science team members. ML acknowledges support of the Swiss National Science Foundation under grant number PCEFP2_194576. PM acknowledges support from STFC research grant number ST/M001040/1. VNa, Ipa, GPi, RRa, and GSc, acknowledge the funding support from Italian Space Agency (ASI) regulated by 'Accordo ASI-INAF n. 2013-016-R.0 del 9 luglio 2013 e integrazione del 9 luglio 2015 CHEOPS Fasi A/B/C'.

This work was also partially supported by a grant from the Simons Foundation (PI Queloz, grant number 327127). IRI acknowledges support from the Spanish Ministry of Science and Innovation and the European Regional Development Fund through grant PGC2018-098153-B-C33, as well as the support of the Generalitat de Catalunya/CERCA programme. SS has received funding from the European Research Council (ERC) under the European Union's Horizon 2020 research and innovation programme (grant agreement No 833925, project STAREX). GyMSz acknowledges the support of the Hungarian National Research, Development and Innovation Office (NKFIH) grant K-125015, a PRODEX Institute Agreement between the ELTE Eötvös Loránd University and the European Space Agency (ESA-D/SCI-LE-2021-0025), the Lendület LP2018-7/2021 grant of the Hungarian Academy of Science and the support of the city of Szombathely. VVG is an F.R.S-FNRS Research Associate. DB has been funded by the Spanish State Research Agency (AEI) Projects No. PID2019-107061GB-C61 and No. MDM-2017-0737 Unidad de Excelencia 'María de Maeztu'-Centro de Astrobiología (CSIC/INTA).

DATA AVAILABILITY

The *TESS* data are accessible via the MAST (Mikulski Archive for Space Telescopes) portal at https://mast.stsci.edu/portal/Mashup/Clients/Mast/Portal.html. Photometry and imaging data from *NGTS*, *MEarth*, *LCOGT*, *ASTEP*, and *Gemini* are accessible via the ExoFOP-*TESS* archive at https://exofop.ipac.caltech.edu/tess/target.php?id = 440887364. The `exoplanet` modelling code and associated `python` scripts for parameter analysis and plotting are available upon reasonable request to the author. The posterior plots are available online as supplementary material to this publication.

REFERENCES

Abe L. et al., 2013, A&A, 553, A49
Addison B. et al., 2019, PASP, 131, 115003
Addison B. C. et al., 2021, MNRAS, 502, 3704
Adibekyan V. Z., Sousa S. G., Santos N. C., Delgado Mena E., González Hernández J. I., Israelian G., Mayor M., Khachatryan G., 2012, A&A, 545, A32
Adibekyan V. et al., 2015, A&A, 583, A94
Adibekyan V. et al., 2021, Science, 374, 330
Agol E., Luger R., Foreman-Mackey D., 2020, AJ, 159, 123
Akeson R. L. et al., 2013a, PASP, 125, 989
Akeson R. et al., 2013b, PASP, 125, 989
Aller A., Lillo-Box J., Jones D., Miranda L. F., Barceló Forteza S., 2020, A&A, 635, A128
Astropy Collaboration 2013, A&A, 558, A33
Astropy Collaboration 2018, AJ, 156, 123
Auvergne M. et al., 2009, A&A, 506, 411
Bakos G. Á. et al., 2013, PASP, 125, 154
Bakos G., Noyes R. W., Kovács G., Stanek K. Z., Sasselov D. D., Domsa I., 2004, PASP, 116, 266
Batalha N. et al., 2021, Seeing the Forest and the Trees: Unveiling Small Planet Atmospheres with a Population-Level Framework, JWST Proposal. Cycle 1
Bensby T., Feltzing S., Lundström I., 2003, A&A, 410, 527
Bensby T., Feltzing S., Oey M. S., 2014, A&A, 562, A71
Benz W. et al., 2021, Exp. Astron., 51, 109
Blackwell D. E., Shallis M. J., 1977, MNRAS, 180, 177
Bonfanti A., Ortolani S., Piotto G., Nascimbeni V., 2015, A&A, 575, A18
Bonfanti A., Ortolani S., Nascimbeni V., 2016, A&A, 585, A5
Bonfanti A. et al., 2021, A&A, 646, A157
Borucki W. J. et al., 2010, Science, 327, 977
Brown T. M. et al., 2013, PASP, 125, 1031
Bryant E. M. et al., 2020, MNRAS, 494, 5872
Buchhave L. A. et al., 2012, Nature, 486, 375
Buchhave L. A. et al., 2014, Nature, 509, 593
Butler R. P., Marcy G. W., Williams E., McCarthy C., Dosanjh P., Vogt S. S., 1996, PASP, 108, 500
Butler R. P. et al., 2017, AJ, 153, 208
Cale B. L. et al., 2021, AJ, 162, 295
Castelli F., Kurucz R. L., 2003, in Piskunov N., Weiss W. W., Gray D. F., eds, Proc. IAU Symp. 210, Modelling of Stellar Atmospheres. Cambridge Univ. Press, Cambridge, p. A20
Celisse A., 2008, preprint (arXiv:0811.0802)
Chen D.-C. et al., 2021, ApJ, 909, 115
Chen D.-C. et al., 2022, AJ, 163, 249
Ciardi D. R., Beichman C. A., Horch E. P., Howell S. B., 2015, ApJ, 805, 16
Cloutier R., Menou K., 2020, AJ, 159, 211
Cloutier R. et al., 2020, AJ, 160, 22
Collins K. A., Kielkopf J. F., Stassun K. G., Hessman F. V., 2017, AJ, 153, 77
Crane J. D., Shectman S. A., Butler R. P., 2006, in McLean I. S., Iye M., eds, Proc. SPIE Conf. Ser. Vol. 6269, Ground-based and Airborne Instrumentation for Astronomy. SPIE, Bellingham, p. 626931
Crane J. D., Shectman S. A., Butler R. P., Thompson I. B., Burley G. S., 2008, in McLean I. S., Casali M. M., eds, Proc. SPIE Conf. Ser. Vol. 7014, Ground-based and Airborne Instrumentation for Astronomy II. SPIE, Bellingham, p. 701479
Crane J. D., Shectman S. A., Butler R. P., Thompson I. B., Birk C., Jones P., Burley G. S., 2010, in McLean I. S., Ramsay S. K., Takami H., eds, Proc. SPIE Conf. Ser. Vol. 7735, Ground-based and Airborne Instrumentation for Astronomy III. SPIE, Bellingham, p. 773553
Crouzet N. et al., 2010, A&A, 511, A36
Crouzet N. et al., 2018, A&A, 619, A116
Crouzet N. et al., 2020, in Evans C. J., Bryant J. J., Motohara K., eds, Proc. SPIE Conf. Ser. Vol. 11447: Ground-based and Airborne Instrumentation for Astronomy VIII. SPIE, Bellingham, p. 114470O
Daban J.-B. et al., 2010, in Stepp L. M., Gilmozzi R., Hall H. J., eds, Proc. SPIE Conf. Ser. Vol. 7733, Ground-based and Airborne Telescopes III. SPIE, Bellingham, p. 77334T
Delgado Mena E., Adibekyan V., Santos N. C., Tsantaki M., González Hernández J. I., Sousa S. G., Bertrán de Lis S., 2021, A&A, 655, A99
Delrez L. et al., 2021, Nat. Astron., 5, 775
Eastman J., Gaudi B. S., Agol E., 2013, PASP, 125, 83
Eastman J. D. et al., 2019, preprint (arXiv:1907.09480)
Fabrycky D. C. et al., 2014, ApJ, 790, 146
Fang J., Margot J.-L., 2012, ApJ, 761, 92
Figueira P. et al., 2012, A&A, 541, A139
Foreman-Mackey D., Agol E., Ambikasaran S., Angus R., 2017, celerite: Scalable 1D Gaussian Processes in C++, Python, and Julia, record ascl:1709.008
Foreman-Mackey D. et al., 2021a, exoplanet-dev/exoplanet: exoplanet v0.4.5. https://doi.org/10.5281/zenodo.4604868
Foreman-Mackey D. et al., 2021b, exoplanet-dev/exoplanet v0.4.5. https://doi.org/10.5281/zenodo.1998447
Foreman-Mackey D. et al., 2021c, preprint (arXiv:2105.01994)
Fressin F. et al., 2005, in Giard M., Casoli F., Paletou F., eds, EAS Publications Series Vol. 14, EAS Publications Series. p. 309
Fulton B. J., Petigura E. A., 2018, AJ, 156, 264
Fulton B. J. et al., 2017, AJ, 154, 109
Furlan E. et al., 2017, AJ, 153, 71
Fűrész G., 2008, PhD thesis, University of Szeged, Hungary
Gaia Collaboration 2018, A&A, 616, A1
Gaia Collaboration 2021, A&A, 649, A1
Gardner J. P. et al., 2006, Space Sci. Rev., 123, 485
Giacalone S. et al., 2022, AJ, 163, 99
Ginzburg S., Schlichting H. E., Sari R., 2016, ApJ, 825, 29
Grunblatt S. K., Howard A. W., Haywood R. D., 2015, ApJ, 808, 127
Guerrero N. M. et al., 2021, ApJS, 254, 39
Guillot T. et al., 2015, Astron. Nachr., 336, 638

Henden A. A., Templeton M., Terrell D., Smith T. C., Levine S., Welch D., 2016, VizieR Online Data Catalog, 00, II/336
Hoffman M. D., Gelman A., 2011, preprint (arXiv:1111.4246)
Howell S. B., Everett M. E., Sherry W., Horch E., Ciardi D. R., 2011, AJ, 142, 19
Howell S. B. et al., 2014, PASP, 126, 398
Hoyer S., Guterman P., Demangeon O., Sousa S. G., Deleuil M., Meunier J. C., Benz W., 2020, A&A, 635, A24
Irwin J., Irwin M., Aigrain S., Hodgkin S., Hebb L., Moraux E., 2007, MNRAS, 375, 1449
Irwin J. M., Berta-Thompson Z. K., Charbonneau D., Dittmann J., Falco E. E., Newton E. R., Nutzman P., 2015a, 18th Cambridge Workshop on Cool Stars, Stellar Systems, and the Sun. p. 767, preprint (arXiv:1409.0891)
Irwin J., Berta-Thompson Z. K., Charbonneau D., Dittmann J., Newton E. R., 2015b, American Astronomical Society Meeting Abstracts #225, 258.01
Jenkins J. M., 2002, ApJ, 575, 493
Jenkins J. M. et al., 2010, in Radziwill N. M., Bridger A., eds, Proc. SPIE Conf. Ser. Vol. 7740, Software and Cyberinfrastructure for Astronomy. SPIE, Bellingham, p. 77400D
Jenkins J. M. et al., 2016, in Chiozzi G., Guzman J. C., eds, Proc. SPIE Conf. Ser. Vol. 9913, Software and Cyberinfrastructure for Astronomy IV. SPIE, Bellingham, p. 99133E
Jenkins J. M., Tenenbaum P., Seader S., Burke C. J., McCauliff S. D., Smith J. C., Twicken J. D., Chandrasekaran H., 2020, Kepler Data Processing Handbook: Transiting Planet Search, Kepler Science Document KSCI-19081-003.
Jensen E., 2013, Tapir: A web interface for transit/eclipse observability, Astrophysics Source Code Library, record ascl:1306.007
Jin S., Mordasini C., 2018, ApJ, 853, 163
Johansen A., Davies M. B., Church R. P., Holmelin V., 2012, ApJ, 758, 39
Johnson D. R. H., Soderblom D. R., 1987, AJ, 93, 864
Kempton E. M. R. et al., 2018, PASP, 130, 114401
Kipping D. M., 2013a, MNRAS, 434, L51
Kipping D. M., 2013b, MNRAS, 435, 2152
Kumar R., Carroll C., Hartikainen A., Martin O. A., 2019, J. Open Source Softw., 4, 1143
Kurucz R. L., 1993, Phys. Scr. Vol. T, 47, 110
Leleu A. et al., 2021, A&A, 649, A26
Lendl M. et al., 2020, A&A, 643, A94
Li J., Tenenbaum P., Twicken J. D., Burke C. J., Jenkins J. M., Quintana E. V., Rowe J. F., Seader S. E., 2019, PASP, 131, 024506
Lillo-Box J., Barrado D., Bouy H., 2012, A&A, 546, A10
Lillo-Box J., Barrado D., Bouy H., 2014, A&A, 566, A103
Lindegren L. et al., 2021, A&A, 649, A4
Lissauer J. J. et al., 2011, ApJS, 197, 8
Lissauer J. J. et al., 2012, ApJ, 750, 112
Lovis C., Pepe F., 2007, A&A, 468, 1115
Luger R., Agol E., Foreman-Mackey D., Fleming D. P., Lustig-Yaeger J., Deitrick R., 2019, AJ, 157, 64
Marigo P. et al., 2017, ApJ, 835, 77
Martinez C. F., Cunha K., Ghezzi L., Smith V. V., 2019, ApJ, 875, 29
Maxted P. F. L. et al., 2011, PASP, 123, 547
Mayor M., Queloz D., 1995, Nature, 378, 355
Mayor M. et al., 2003, The Messenger, 114, 20
McCully C., Volgenau N. H., Harbeck D.-R., Lister T. A., Saunders E. S., Turner M. L., Siiverd R. J., Bowman M., 2018, in Guzman J. C., Ibsen J., eds, Proc. SPIE Conf. Ser. Vol. 10707, Software and Cyberinfrastructure for Astronomy V. SPIE, Bellingham, p. 107070K
Mékarnia D. et al., 2016, MNRAS, 463, 45
Millholland S. C., Winn J. N., 2021, ApJ, 920, L34
Millholland S., Wang S., Laughlin G., 2017, ApJ, 849, L33
Nesvorný D., Kipping D., Terrell D., Feroz F., 2014, ApJ, 790, 31
Osborn A. et al., 2021, MNRAS, 507, 2782
Owen J. E., Wu Y., 2013, ApJ, 775, 105
Pepper J. et al., 2007, PASP, 119, 923
Pollacco D. L. et al., 2006, PASP, 118, 1407
Rayner J., Bond T., Bonnet M., Jaffe D., Muller G., Tokunaga A., 2012, in McLean I. S., Ramsay S. K., Takami H., eds, Proc. SPIE Conf. Ser. Vol. 8446, Ground-based and Airborne Instrumentation for Astronomy IV. SPIE, Bellingham, p. 84462C
Reddy B. E., Lambert D. L., Allende Prieto C., 2006, MNRAS, 367, 1329
Ricker G. R. et al., 2015, J. Astron. Telesc. Instrum. Syst., 1, 014003
Rousset G. et al., 2003, in Wizinowich P. L., Bonaccini D., eds, Proc. SPIE Conf. Ser. Vol. 4839, Adaptive Optical System Technologies II. SPIE, Bellingham, p. 140
Salmon S. J. A. J., Van Grootel V., Buldgen G., Dupret M. A., Eggenberger P., 2021, A&A, 646, A7
Salvatier J., Wiecki T. V., Fonnesbeck C., 2016, PeerJ Comput. Sci., 2, e55
Santerne A. et al., 2018, Nat.Astron., 2, 393
Santos N. C. et al., 2013, A&A, 556, A150
Schanche N. et al., 2020, MNRAS, 499, 428
Schlichting H. E., Sari R., Yalinewich A., 2015, Icarus, 247, 81
Scott N. J. et al., 2021, Front. Astron. Space Sci., 8, 138
Scuflaire R., Théado S., Montalbán J., Miglio A., Bourge P.-O., Godart M., Thoul A., Noels A., 2008, Ap&SS, 316, 83
Skrutskie M. F. et al., 2006, AJ, 131, 1163
Smith J. C. et al., 2012, PASP, 124, 1000
Smith A. M. S. et al., 2020, Astron. Nachr., 341, 273
Sneden C. A., 1973, PhD thesis, The University of Texas at Austin
Sousa S. G., 2014, in Banaszkiewicz M., Węsławski J. M., Lewandowski M., Sarna M., eds, GeoPlanet: Earth and Planetary Sciences. Springer, Berlin, p. 297
Sousa S. G., Santos N. C., Adibekyan V., Delgado-Mena E., Israelian G., 2015, A&A, 577, A67
Sousa S. G. et al., 2021, A&A, 656, A53
Southworth J., 2011, MNRAS, 417, 2166
Stassun K. G. et al., 2019, AJ, 158, 138
Stumpe M. C. et al., 2012, PASP, 124, 985
Stumpe M. C., Smith J. C., Catanzarite J. H., Van Cleve J. E., Jenkins J. M., Twicken J. D., Girouard F. R., 2014, PASP, 126, 100
Teske J. et al., 2021, ApJS, 256, 33
Theano Development Team, 2016, preprint (abs/1605.02688)
Tremaine S., Dong S., 2012, AJ, 143, 94
Twicken J. D. et al., 2018, PASP, 130, 064502
Van Eylen V., Agentoft C., Lundkvist M. S., Kjeldsen H., Owen J. E., Fulton B. J., Petigura E., Snellen I., 2018, MNRAS, 479, 4786
Van Eylen V. et al., 2021, MNRAS, 507, 2154
Vogt S. S., Penrod G. D., 1988, in Robinson L. B., ed., Instrumentation for Ground-Based Optical Astronomy. Springer, New York, p. 68
Wheatley P. J. et al., 2018, MNRAS, 475, 4476
Wilson T. G. et al., 2022, MNRAS, 511, 1043
Wittenmyer R. et al., 2018, American Astronomical Society Meeting Abstracts #231, 128.01
Wright E. L. et al., 2010, AJ, 140, 1868
Zeng L., Sasselov D. D., Jacobsen S. B., 2016, ApJ, 819, 127
Ziegler C., Tokovinin A., Briceño C., Mang J., Law N., Mann A. W., 2020, AJ, 159, 19

SUPPORTING INFORMATION

Supplementary data are available at *MNRAS* online.

Please note: Oxford University Press is not responsible for the content or functionality of any supporting materials supplied by the authors. Any queries (other than missing material) should be directed to the corresponding author for the article.

APPENDIX A: PRIORS

Table A1. Global fit parameter prior function type and prior limits for TOI-836.

Parameter	Prior	Value
Baseline flux	$\mathcal{N}(0, 1)$	
M_* ($M_\odot$)	$\mathcal{N}(0.678, 0.049, 0.65)$	Table 6
R_* ($R_\odot$)	$\mathcal{N}(0.666, 0.010, 0.56)$	Table 6
Period (d)	$\mathcal{N}(22, 0.1)$	Table 6
LD coefficient u_1	Kipping (2013b)	Table 6
LD coefficient u_2	Kipping (2013b)	Table 6
TESS GP		
Sector 11		
Mean	$\mathcal{N}(0, 1)$	0.00006 ± 0.00021
log($s2$)	$\mathcal{N}$(-14.704*, 0.1)	-14.98064 ± 0.01205
log($w0$)	$\mathcal{N}(0, 0.1)$	0.10400 ± 0.09697
log($Sw4$)	$\mathcal{N}$(-14.704*, 0.1)	-14.12245 ± 0.09004
Sector 38		
Mean	$\mathcal{N}(0, 1)$	0.00008 ± 0.00031
log($s2$)	$\mathcal{N}$(-13.903*, 0.1)	-14.86420 ± 0.01063
log($w0$)	$\mathcal{N}(0, 0.05)$	0.00736 ± 0.04815
log($Sw4$)	$\mathcal{N}$(-13.903*, 0.1)	-13.47408 ± 0.04995
RV GP		
Amplitude	$\mathcal{C}(5)$	7.13782 ± 1.05463
l_E	$\mathcal{T}(22, 20, 20)$	31.59616 ± 5.63098
l_P	$\mathcal{T}(0.1, 10, 0, 1)$	0.21018 ± 0.02573
HARPS offset	$\mathcal{N}$(-26274.131†,10)	-26144.6 ± 2622.4
log(Jitter)$_{HARPS}$	$\mathcal{N}$(0.247‡,5)	-3.01818 ± 3.12178
PFS offset	$\mathcal{N}$(0.403†,10)	-0.75678 ± 1.72435
log(Jitter)$_{PFS}$	$\mathcal{N}$(-1.270‡,5)	-1.51981 ± 3.07024

Notes. **Prior distributions:**
(lower limit x, upper limit y) for uniform distribution $\mathcal{U}(x,y)$.
(mean μ, standard deviation σ, test value α) for normal distribution $\mathcal{N}(\mu, \sigma, \alpha)$.
(mean μ, standard deviation σ, lower limit x, upper limit y) for truncated normal distribution $\mathcal{T}(\mu, \sigma, x, y)$.
(scale parameter β) for half-Cauchy distribution $\mathcal{C}(\beta)$.
Prior values:
* Equivalent to the log of the variance of the *TESS* flux from the corresponding sector.
† Equivalent to the mean of the radial velocity from the corresponding spectrographs.
‡ Equivalent to 2 times the log of the minimum radial velocity error from the corresponding spectrographs.

Table A2. Global fit parameter prior function type and prior limits for TOI-836 b.

Parameter	Prior
TOI-836 b	
Period (d)	$\mathcal{U}(3.7, 3.9)$
Transit ephemeris (TBJD)	$\mathcal{U}(2458599.98, 2458600.03)$
K_{RV} ($m\,s^{-1}$)	$\mathcal{U}(0, 10)$
log(R_p)	$\mathcal{N}$(-4.062Section 1)
b	$\mathcal{U}(0, 1)$
e	Kipping (2013a), $\mathcal{B}$(e, 0.867, 3.03)
ω (rad)	$\mathcal{U}(-\pi, \pi)$

Notes. Numbers in brackets represent:
(lower limit x, upper limit y) for uniform distribution $\mathcal{U}(x,y)$.
(mean μ, standard deviation σ, test value α) for normal distribution $\mathcal{N}(\mu, \sigma, \alpha)$.
Distributions for eccentricity e are built into the `exoplanet` package and based on Kipping (2013a) which includes the Beta distribution $\mathcal{B}$(e,a,b) (exponential e, shape parameter a, shape parameter b).
§ Equivalent to $0.5\times\log(\delta) + \log(R_*)$, δ represents transit depth (based on ExoFOP catalogue values).

Table A3. Global fit parameter prior function type and prior limits for TOI-836 c.

Parameter	Prior
TOI-836 c	
Period (d)	$\mathcal{U}(8.5, 8.7)$
Transit ephemeris (TBJD)	$\mathcal{U}(2458599.74, 2458599.79)$
K_{RV} ($m\,s^{-1}$)	$\mathcal{U}(0, 10)$
log(R_p)	$\mathcal{N}(-3.701$ Section 1)
b	$\mathcal{U}(0, 1)$
e	Kipping (2013a), $\mathcal{B}$(e, 0.867, 3.03)
ω (rad)	$\mathcal{U}(-\pi, \pi)$

Notes. Numbers in brackets represent:
(lower limit x, upper limit y) for uniform distribution $\mathcal{U}(x,y)$.
(mean μ, standard deviation σ, test value α) for normal distribution $\mathcal{N}(\mu, \sigma, \alpha)$.
Distributions for eccentricity e are built into the `exoplanet` package and based on Kipping (2013a) which includes the Beta distribution $\mathcal{B}$(e,a,b) (exponential e, shape parameter a, shape parameter b).
§ Equivalent to $0.5\times\log(\delta) + \log(R_*)$, δ represents transit depth (based on ExoFOP catalogue values).

[1]*Department of Physics, University of Warwick, Gibbet Hill Road, Coventry CV4 7AL, UK*
[2]*Centre for Exoplanets and Habitability, University of Warwick, Gibbet Hill Road, Coventry CV4 7AL, UK*
[3]*Centre for Exoplanet Science, SUPA School of Physics and Astronomy, University of St Andrews, North Haugh, St Andrews KY16 9SS, UK*
[4]*Space Research Institute, Austrian Academy of Sciences, Schmiedlstrasse 6, A-8042 Graz, Austria*
[5]*Instituto de Astrofísica e Ciências do Espaço, Universidade do Porto, CAUP, Rua das Estrelas, P-4150-762 Porto, Portugal*
[6]*Departamento de Física e Astronomia, Faculdade de Ciências, Universidade do Porto, Rua do Campo Alegre, P-4169-007 Porto, Portugal*
[7]*Physikalisches Institut, University of Bern, Gesellsschaftstrasse 6, CH-3012 Bern, Switzerland*
[8]*Center for Astrophysics, Harvard and Smithsonian, 60 Garden St., Cambridge, MA 02138, USA*
[9]*Université Côte d'Azur, Observatoire de la Côte d'Azur, CNRS, Laboratoire Lagrange, CS 34229, F-06304 Nice Cedex 4, France*
[10]*School of Physics and Astronomy, University of Leicester, Leicester LE1 7RH, UK*
[11]*University of Southern Queensland, Centre for Astrophysics, USQ Toowoomba, West Street, QLD 4350, Australia*
[12]*Instituto de Astrofisica de Canarias, E-38200 La Laguna, Tenerife, Spain*
[13]*Departamento de Astrofisica, Universidad de La Laguna, E-38206 La Laguna, Tenerife, Spain*
[14]*Departamento de Astronomia, Universidad de Chile, Casilla 36-D, Santiago, Chile*
[15]*Institut de Ciencies de l'Espai (ICE, CSIC), Campus UAB, Can Magrans s/n, E-08193 Bellaterra, Spain*
[16]*Institut d'Estudis Espacials de Catalunya (IEEC), E-08034 Barcelona, Spain*
[17]*Admatis, 5. Kandó Kálmán Street, 3534 Miskolc, Hungary*
[18]*NASA Goddard Space Flight Center, 8800 Greenbelt Road, Greenbelt, MD 20771, USA*
[19]*Department of Physics, University of Maryland, Baltimore County, 1000 Hilltop Circle, Baltimore, MD 21250, USA*
[20]*Depto. de Astrofísica, Centro de Astrobiología (CSIC-INTA), ESAC campus, E-28692 Villanueva de la Cañada (Madrid), Spain*
[21]*Center for Space and Habitability, Gesellsschaftstrasse 6, CH-3012 Bern, Switzerland*
[22]*Université Grenoble Alpes, CNRS, IPAG, F-38000 Grenoble, France*
[23]*Observatoire de Genève, Université de Genève, Chemin de Pegasi, 51, CH-1290 Versoix, Switzerland*

[24]*Department of Astronomy, Stockholm University, AlbaNova University Center, SE-10691 Stockholm, Sweden*
[25]*Programma Nazionale di Ricerche in Antartide (PNRA), Concordia station, V8XW+WG4, Antarctica*
[26]*Institute of Planetary Research, German Aerospace Center (DLR), Rutherfordstrasse 2, D-12489 Berlin, Germany*
[27]*SETI Institute/NASA Ames Research Center, Moffett Field, CA 94035, USA*
[28]*Université de Paris, Institut de physique du globe de Paris, CNRS, F-75005 Paris, France*
[29]*Department of Physics, George Mason University, 4400 University Drive, Fairfax, VA 22030, USA*
[30]*American Association of Variable Star Observers, 49 Bay State Road, Cambridge, MA 02138, USA*
[31]*European Space Agency (ESA), European Space Research and Technology Centre (ESTEC), Keplerlaan 1, NL-2201 AZ Noordwijk, the Netherlands*
[32]*Centre for Mathematical Sciences, Lund University, Box 118, SE-221 00 Lund, Sweden*
[33]*Aix Marseille Univ, CNRS, CNES, LAM, 38 rue Frédéric Joliot-Curie, F-13388 Marseille, France*
[34]*Astrobiology Research Unit, Université de Liège, Allée du 6 Août 19C, B-4000 Liège, Belgium*
[35]*Space sciences, Technologies and Astrophysics Research (STAR) Institute, Université de Liège, Allée du 6 Août 19C, B-4000 Liège, Belgium*
[36]*School of Physics and Astronomy, University of Birmingham, Edgbaston, Birmingham B15 2TT, UK*
[37]*Department of Earth, Atmospheric and Planetary Sciences, Massachusetts Institute of Technology, Cambridge, MA 02139, USA*
[38]*Department of Physics and Kavli Institute for Astrophysics and Space Research, Massachusetts Institute of Technology, Cambridge, MA 02139, USA*
[39]*Leiden Observatory, University of Leiden, PO Box 9513, NL-2300 RA Leiden, the Netherlands*
[40]*Department of Space, Earth and Environment, Chalmers University of Technology, Onsala Space Observatory, SE-43992 Onsala, Sweden*
[41]*Department of Astrophysics, University of Vienna, Türkenschanzstrasse 17, A-1180 Vienna, Austria*
[42]*Dipartimento di Fisica, Universita degli Studi di Torino, via Pietro Giuria 1, I-10125 Torino, Italy*
[43]*NASA Ames Research Center, Moffett Field, CA 94035, USA*
[44]*NASA Exoplanet Science Institute, Caltech/IPAC, Mail Code 100-22, 1200 E. California Blvd., Pasadena, CA 91125, USA*
[45]*Astrophysics Group, Keele University, Keele ST5 5BG, UK*
[46]*Cavendish Laboratory, JJ Thomson Avenue, Cambridge CB3 0HE, UK*
[47]*Núcleo de Astronomía, Facultad de Ingeniería y Ciencias, Universidad Diego Portales, Av. Ejército 441, Santiago, Chile*
[48]*Centro de Astrofísica y Tecnologías Afines (CATA), Casilla 36-D, Santiago, Chile*
[49]*Department of Physics and Astronomy, Swarthmore College, Swarthmore, PA 19081, USA*
[50]*Department of Earth and Planetary Sciences, University of California, Riverside, CA 92521, USA*
[51]*Department of Physics and Astronomy, University of Louisville, Louisville, KY 40292, USA*
[52]*Konkoly Observatory, Research Centre for Astronomy and Earth Sciences, 1121 Budapest, Konkoly Thege Miklós út 15-17, Hungary*
[53]*ELTE Eötvös Loránd University, Institute of Physics, Pázmány Péter sétány 1/A, 1117 Budapest, Hungary*
[54]*INAF, Osservatorio Astronomico di Padova, Vicolo dell'Osservatorio 5, I-35122 Padova, Italy*
[55]*IMCCE, UMR8028 CNRS, Observatoire de Paris, PSL Univ., Sorbonne Univ., 77 av. Denfert-Rochereau, F-75014 Paris, France*
[56]*Institut d'astrophysique de Paris, UMR7095 CNRS, Université Pierre & Marie Curie, 98bis blvd. Arago, F-75014 Paris, France*
[57]*Villa '39 Observatory, Landers, CA 92285, USA*
[58]*European Southern Observatory, Karl-Schwarzschildstrasse 2, D-85748 Garching bei München, Germany*
[59]*Astrophysics Research Centre, School of Mathematics and Physics, Queen's University Belfast, Belfast BT7 1NN, UK*
[60]*INAF, Osservatorio Astrofisico di Catania, Via S. Sofia 78, I-95123 Catania, Italy*
[61]*Chalmers University of Technology, Chalmersplatsen 4, SE-412 96 G'oteborg, Sweden*
[62]*Dipartimento di Fisica e Astronomia 'Galileo Galilei', Universita degli Studi di Padova, Vicolo dell'Osservatorio 3, I-35122 Padova, Italy*
[63]*ETH Zurich, Department of Physics, Wolfgang-Pauli-Strasse 2, CH-8093 Zurich, Switzerland*
[64]*Cavendish Laboratory, JJ Thomson Avenue, Cambridge CB3 0HE, UK*
[65]*Center for Astronomy and Astrophysics, Technical University Berlin, Hardenberstrasse 36, D-10623 Berlin, Germany*
[66]*Institut für Geologische Wissenschaften, Freie Universitãt Berlin, D-12249 Berlin, Germany*
[67]*Patashnick Voorheesville Observatory, Voorheesville, NY 12186, USA*
[68]*Kotizarovci Observatory, Sarsoni 90, 51216 Viskovo, Croatia*
[69]*ELTE Eötvös Loránd University, Gothard Astrophysical Observatory, 9700 Szombathely, Szent Imre h. u. 112, Hungary*
[70]*MTA-ELTE Exoplanet Research Group, 9700 Szombathely, Szent Imre h. u. 112, Hungary*
[71]*Earth and Planets Laboratory, Carnegie Institution for Science, 5241 Broad Branch Road NW, Washington, DC 20015, USA*
[72]*Institute of Astronomy, University of Cambridge, Madingley Road, Cambridge CB3 0HA, UK*
[73]*Department of Astronomy, Tsinghua University, Beijing 100084, People's Republic of China*
[74]*Department of Astrophysical Sciences, Princeton University, Princeton, NJ 08544, USA*
[75]*Shanghai Astronomical Observatory, 80 Nandan Road, Shanghai 200030, China*

This paper has been typeset from a TEX/LATEX file prepared by the author.